The Astrophysical Journal, 940:12 (21pp), 2022 November 20 https://doi.org/10.3847/1538-4357/ac922e

The Active Chromospheres of Lithium-rich Red Giant Stars*

Christopher Sneden[1], Melike Afşar[1,2], Zeynep Bozkurt[2], Monika Adamów[3], Anohita Mallick[4], Bacham E. Reddy[4], Steven Janowiecki[5], Suvrath Mahadevan[6,7], Brendan P. Bowler[1], Keith Hawkins[1], Karin Lind[8], Andrea K. Dupree[9], Joe P. Ninan[6,7,10], Neel Nagarajan[1], Gamze Böcek Topcu[2], Cynthia S. Froning[1], Chad F. Bender[11], Ryan Terrien[12], Lawrence W. Ramsey[6,7], and Gregory N. Mace[1]
[1] Department of Astronomy and McDonald Observatory, The University of Texas, Austin, TX 78712, USA; chris@verdi.as.utexas.edu
[2] Department of Astronomy and Space Sciences, Ege University, 35100 Bornova, İzmir, Turkey
[3] Center for AstroPhysical Surveys, National Center for Supercomputing Applications, Urbana, IL 61801, USA
[4] Indian Institute of Astrophysics, Bangalore 560034, India
[5] Hobby Eberly Telescope, The University of Texas, Austin, TX 78712, USA
[6] Department of Astronomy & Astrophysics, The Pennsylvania State University, University Park, PA 16803, USA
[7] Center for Exoplanets and Habitable Worlds, The Pennsylvania State University, University Park, PA 16803, USA
[8] Department of Astronomy, Stockholm University, AlbaNova University Centre, SE-106 91 Stockholm, Sweden
[9] Center for Astrophysics/Harvard & Smithsonian, Cambridge, MA 02138-1516, USA
[10] Department of Astronomy and Astrophysics, Tata Institute of Fundamental Research, Homi Bhabha Road, Colaba, Mumbai 400005, India
[11] Steward Observatory, University of Arizona, Tucson, AZ 85721, USA
[12] Department of Physics and Astronomy, Carleton College, Northfield, MN 55057, USA
Received 2022 July 17; revised 2022 September 11; accepted 2022 September 13; published 2022 November 15

Abstract

We have gathered near-infrared *zyJ*-band high-resolution spectra of nearly 300 field red giant stars with known lithium abundances in order to survey their He I λ10830 absorption strengths. This transition is an indicator of chromospheric activity and/or mass loss in red giants. The majority of stars in our sample reside in the red clump or red horizontal branch based on their $V-J$, M_V color–magnitude diagram, and Gaia $T_{\rm eff}$ and log(g) values. Most of our target stars are Li-poor in the sense of having normally low Li abundances, defined here as $\log\epsilon({\rm Li}) < 1.25$. Over 90% of these Li-poor stars have weak λ10830 features. However, more than half of the 83 Li-rich stars ($\log\epsilon({\rm Li}) > 1.25$) have strong λ10830 absorptions. These large λ10830 lines signal excess chromospheric activity in Li-rich stars; there is almost no indication of significant mass loss. The Li-rich giants may also have a higher binary fraction than Li-poor stars, based on their astrometric data. It appears likely that both residence on the horizontal branch and present or past binary interaction play roles in the significant Li–He connection established in this survey.

Unified Astronomy Thesaurus concepts: Stellar spectral lines (1630); Stellar chromospheres (230); Stellar photospheres (1237); Stellar abundances (1577); Red giant stars (1372)

Supporting material: machine-readable table

1. Introduction

Lithium is easily destroyed in stellar interiors as part of the proton–proton fusion cycles. At modest fusion temperatures, $T \geqslant 2.5\times10^6$ K, the reaction $^7{\rm Li}(p,\alpha)\rightarrow{}^4{\rm He}$ efficiently cleans out lithium in interior regions. Then basic stellar evolution computations (e.g., Iben 1967) predict that for metal-rich stars the deepening convective envelopes during subgiant and first-ascent red giant evolution will dilute the initial surface Li abundances by factors approaching ∼60. In this way the stellar age-zero Li contents ($\log\epsilon({\rm Li})\simeq3.3$)[13] that are observed in warm main-sequence stars (Randich et al. 2020; Romano et al. 2021) and in the primordial solar system (Lodders 2021) will be substantially diminished, leaving normal red giants with $\log\epsilon({\rm Li})\sim1.5$. However, few evolved stars have that much surface Li. Decades ago surveys of Li in red giants (e.g., Wallerstein & Conti 1969; Lambert et al. 1980; Brown et al. 1989) established that nearly all red giants have $\log\epsilon({\rm Li}) < 1.0$, and abundance upper limits are common. This is consistent with the small Li abundances in cool main-sequence stars (dating back to Wallerstein & Conti 1969 and Boesgaard & Tripicco 1986, 1987), those with $T_{\rm eff} < 6500$ K. Slow circulation currents during long main-sequence lifetimes deplete the surface Li abundances before stars evolve to become giants. The very low Li content of normal red giant stars is no mystery.

However, about 1% of red giants have unexpectedly strong Li I 6707 Å absorption lines, often leading to Li abundances that are much greater than the maximum values in main-sequence stars. The first serendipitous discovery of a Li-rich giant (Wallerstein & Sneden 1982) has been followed by many other detections; now more than 100 relatively bright Li-rich evolved stars have been cataloged. The origin of this phenomenon is not clear. The best "interior" hypothesis is the so-called beryllium transport mechanism (Cameron & Fowler 1971), in which the reactions $^3{\rm He}(\alpha,\gamma)^7{\rm Be}(e^-,\nu)^7{\rm Li}$ create Li, which then must be quickly convected to the surface before it

* Based on observations obtained with the Hobby–Eberly Telescope, which is a joint project of the University of Texas at Austin, the Pennsylvania State University, Ludwig-Maximilians-Universität München, and Georg-August-Universität Göttingen.

[13] We adopt the standard spectroscopic notation (Wallerstein & Helfer 1959) that for elements A and B, $[{\rm A/B}]\equiv\log_{10}(N_{\rm A}/N_{\rm B})_\star-\log_{10}(N_{\rm A}/N_{\rm B})_\odot$. We use the definition $\log\epsilon({\rm A})\equiv\log_{10}(N_{\rm A}/N_{\rm H})+12.0$ and equate the metallicity with the stellar [Fe/H] value.

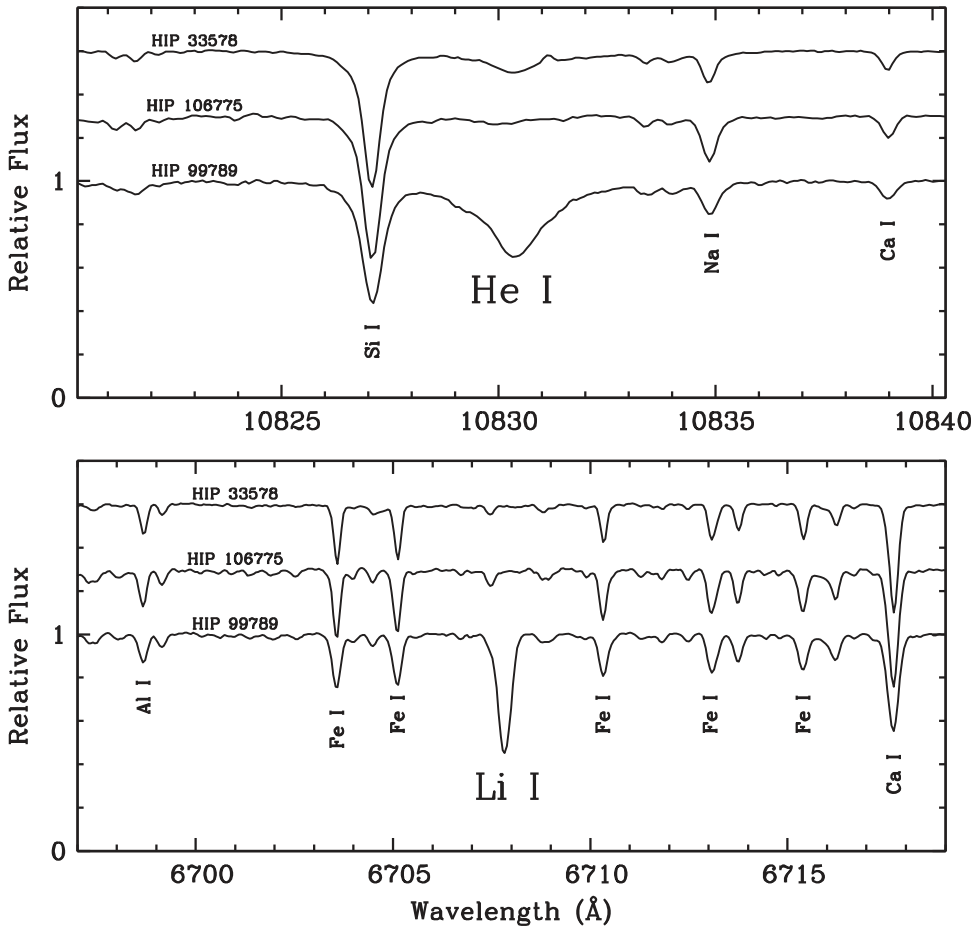

Figure 1. Top panel: He I 10830 Å spectra of three red horizontal-branch stars (Sneden et al. 2021). Bottom panel: +Li I 6707 Å resonance feature in these stars (Afšar et al. 2018; Z. Bozkurt et al. 2022, in preparation).

can decay by capturing a proton as described above. The most prominent "exterior" hypothesis invokes terrestrial or hot-Jupiter planet engulfment by stars (Alexander 1967) as they bloat themselves at post-main-sequence life stages.

The observational clues are mixed, but recent evidence appears to favor the interior production and mixing explanation. The Adamów et al. (2014) spectroscopic red giant survey found that their four most Li-rich giants (log ϵ(Li) > 1.5) either have low-mass companions or significant radial velocity variations, suggesting that companions play roles in the Li-enrichment processes. However, Singh et al. (2019a) used asteroseismic and spectroscopic analyses of more than 10,000 giants to show that nearly all of the very Li-rich giants in their survey are in the He-core-burning red clump (RC) stage. Casey et al. (2019) combined these ideas to suggest that tidal interactions between (primarily) He-core-burning RC giants and binary companions can induce internal mixing to bring newly created Li to the stellar surfaces for brief ($\sim 10^6$ yr) episodes. Using the controlled large sample the study by Kumar et al. (2020) demonstrated the ubiquitous presence of Li-rich giants among He-core burning RC giants making a case for Li enhancement during the He-flash. Singh et al. (2021) have now shown that very high Li abundances are associated with "young" He-core-burning giants that have just recently arrived on the clump following the RGB-tip He flash. Finally, Deepak & Reddy (2020) argue that the lack of correlation of red giant Li abundances with the rotational velocity means that mergers and tidal interactions are unassociated with Li enhancements. However, the large survey by Mallick et al. (2022) for IR excess among RC stars shows that Li-rich giants with IR excess are more likely to be fast rotators compared to Li-normal giants.

Recently Sneden et al. (2021) used the Habitable-zone Planet Finder (hereafter HPF) on the Hobby–Eberly Telescope (HET) to conduct a *zyJ* high-resolution spectroscopic investigation of some red horizontal branch (RHB), or secondary RC field giants. That study discovered a strong He I 10830 Å line in the Li-rich RHB star HIP 99789. We illustrate the Li and He spectral features in HIP 99789 and two other RHB's in Figure 1. The lower excitation energy of the He I 10830 Å transition is 19.8 eV; thus this line cannot be formed in the cool photospheric layers that yield Li I resonance line absorption. Strong λ10830 transitions in cool giant stars signal either excess chromospheric activity or outer atmospheric wind outflow. The notion that He I absorption might be a new clue to the Li-rich giant phenomenon has led us to a survey of He I transitions in Li-rich and Li-poor red giants that we report in this paper.

In this survey the first goal was to discover the fraction of Li-rich giants that have large λ10830 features. Then we looked for correlations between He I absorption and other stellar parameters to help clarify the roles of Galactic population, rotation, chromospheric activity, and stellar/planetary companions on the appearance of strong He I absorption and/or excess Li in

Table 1
Program Star Data

Star	HD or BD	V[a]	$B-V$[a]	$V-J$[a]	p[b] (mas)	log ϵ(Li)	Source	EW$_{He}$ (mÅ)	Broadening[c] (km s^{-1})
TYC 0014-00882-1	BD+04 112	9.89	1.21	2.17	0.819	−0.2	2	115	0.25
TYC 0036-01321-1	HD 12203	6.76	1.02	1.73	5.999	2.0	4	80	0.27
TYC 0037-00427-1	HD 12513	7.55	0.94	1.58	4.150	−1.1	1	50	0.28
TYC 0074-01190-1	HD 26573	6.57	0.91	1.60	8.728	1.4	1	551	0.32
TYC 0096-00109-1	BD+06 750	9.85	1.03	1.83	2.032	0.3	2	303	0.29
TYC 0096-00163-1	⋯	10.43	1.08	1.94	1.699	0.8	2	100	0.27
TYC 0096-00301-1	⋯	9.89	1.14	2.05	1.647	−0.2	2	85	0.25
TYC 0096-00378-1	⋯	10.36	0.92	2.03	1.410	0.3	2	72	0.28
TYC 0096-00659-1	HD 30897	8.26	1.28	2.02	3.666	1.0	2	125	0.24
TYC 0096-00708-1	⋯	10.24	1.02	1.89	1.470	0.3	2	70	0.28

Notes.
[a] Magnitudes and colors are taken from SIMBAD (Wenger et al. 2000).
[b] Parallaxes are from Gaia EDR3 (Gaia Collaboration et al. 2020).
[c] If the value is <1 km s^{-1} then the synthetic spectrum broadening function is a Gaussian with the listed FWHM. If it is >1 km s^{-1}, then the estimated rotational Vsin(i) is listed. See the text for further comments.
References. (1) Z. Bozkurt et al. (to be submitted), (2) Adamów et al. (2014), (3) Mott et al. (2017), (4) Kumar et al. (2011), (5) Brown et al. (1989), (6) Wallerstein & Sneden (1982), (7) Adamów et al. (2015), (8) Balachandran et al. (2000), (9) Hanni (1984), (10) Deepak (2019), (11) Adamów et al. (2018), (12) Luck (1982), (13) Singh et al. (2019a), (14) Zhou et al. (2018), (15) Reddy & Lambert (2016), (16) de Laverny et al. (2003), (17) Yan et al. (2018), (18) Singh et al. (2019b), (19) Singh et al. (2021), (20) Bizyaev et al. (2010), (21) Carlberg et al. (2012), (22) Costa et al. (2015), (23) Yan et al. (2021), (24) N. Nagarajan et al. (2022, to be submitted).

(This table is available in its entirety in machine-readable form.)

giant stars. In Section 2 we describe the stellar sample, and in Section 3 we outline the observations and spectroscopic reduction steps. Section 4 presents the process we used to isolate the λ10830 chromospheric lines from the photospheric spectra, to measure their equivalent widths, and to estimate stellar line broadening. We give the basic results in Section 5, using Li–He correlations to define empirical regions of Li abundance and He-absorption-line strength, and suggest that in all but one case the He lines indicate chromospheric activity rather than mass loss. Correlations of He strengths with space and possible binary motions are presented in Section 6, and we summarize our work in Section 7.

2. The Stellar Sample

Lithium abundances in evolved stars range over at least 5 orders of magnitude, but almost all red giants have log ϵ(Li) < 1.5. Therefore we initially adopted log ϵ(Li) = 1.5 as the upper limit for evolved stars that have suffered the Li destruction, envelope mixing, and surface dilution expected during ordinary stellar evolution. For simplicity in this paper we label all such normal Li-depleted red giants as "Li-poor" stars. Evolved red giants with Li abundances above this limit are given the blanket label "Li-rich." This empirical definition will be reconsidered in Section 5.

Li-rich giant stars have been reported in individual spectroscopic studies (e.g., Luck 1982; Wallerstein & Sneden 1982; Balachandran et al. 2000) and in large-sample Li discovery surveys (e.g., Brown et al. 1989; Kumar et al. 2011; Adamów et al. 2014; Casey et al. 2019; Deepak 2019). We searched the growing literature on this phenomenon and developed a target list based on the following criteria.

1. Confirmed evolved-star status. In general this included stars that are cool ($T_{\rm eff} \lesssim 5500$ K, or $B-V \gtrsim 0.8$) and well off the main sequence (log(g) < 3.5, or $M_V < +1.0$).
2. Sky location in the HET-accessible domain, which is set by its decl. limits: $-10° \lesssim \delta \lesssim +71°$.
3. Target brightness reasonable for HPF. The apparent magnitude bright limit is $J > 3.0$ mag, driven by the need to avoid HPF detector saturation. The practical faint limit is $J \sim 13.0$, to achieve a signal-to-noise ratio (SNR) of SNR > 30 in a total observing time of several hours.[14]

For Li-poor stars we primarily used two large high-resolution optical spectroscopic surveys of field red giants. Adamów et al. (2014) determined Li abundances for 348 stars as part of the Penn State-Toruń Centre for Astronomy Planet Search program; see also atmospheric parameter and overall chemical abundance studies by Zieliński et al. (2012) and Niedzielski et al. (2016). These G–K giants lie in the atmospheric parameter range 4000 K $\lesssim T_{\rm eff} \lesssim$ 5100 K, $-3.0 \lesssim M_V \lesssim 3.0$.

We also observed some red horizontal-branch stars, alternatively called the secondary red clump (Girardi et al. 1998), from the Afşar et al. (2018) 340-star survey. Li abundances for these stars will be published by Z. Bozkurt et al. (2022, in preparation). These two large samples have Li abundances derived in a uniform manner, which is important for those stars with very weak Li I λ6707 features.

When early observations revealed that Li-rich stars can also be rapidly rotating red giants (Vsin(i) $\gtrsim 7$ km s^{-1}), we added some extra targets with substantial rotation from several literature sources: Bizyaev et al. (2010), Carlberg et al. (2012), and Costa et al. (2015). These papers provided some bright stars for relatively easy HPF spectrum acquisition, but do not constitute a comprehensive list of rapidly rotating G–K giants.

In Table 1 we list basic data for the program stars, and the most important measured quantities in this study. The original Li abundance papers used a variety of names for these stars. Almost all of our survey red giants have identifications in the Tycho-2 catalog (Høg et al. 2000).[15] We adopt these "TYC"

[14] For a more complete discussion of HPF integration times see https://psuastro.github.io/HPF/Exposure-Times/.
[15] https://www.cosmos.esa.int/web/Hipparcos/tycho-2

designations throughout this paper when possible. However, many discovery papers on Li-rich red giants have focused on relatively bright stars and have identified them with more traditional names from the HD or BD catalogs. Therefore we also include in Table 1 the HD numbers when available; otherwise we use the BD numbers when possible. There are 278 program stars entered in Table 1. Of this total, 76 stars are Li-rich according to the tentative definition discussed above, 187 stars are Li-poor, and 15 stars have no Li abundance.

Some of the program stars have more than one published Li abundance. Our work with the He I λ10830 transition does not require detailed assessment of literature Li values, so for this paper we have cited a single Li reference in Table 1 for each star. We have not undertaken any renormalization of the abundances and quote log ϵ(Li) to just one significant digit in the table.

Table 1 also contains two additional sets of stars that are special-purpose targets. The first group are red giant members of NGC 7789. This is an open cluster with intermediate age ($t \sim 1.7$ Gyr; WEBDA, Mermilliod 1995)[16] and solar metallicity (e.g., Overbeek et al. 2015, Donor et al. 2018, Carrera et al. 2019, Casamiquela et al. 2019). Pilachowski (1986) discovered that NGC 7789 hosts one and possibly two Li-rich giants, which made this cluster an attractive target for our λ10830 survey. We obtained spectra for 10 of Pilachowski's red giants, and we tabulate here our λ10830 measurements for them, identifying them by cluster and star name. However, we defer discussion of these data to a more general study that contains new optical high-resolution spectra for this cluster (N. Nagarajan et al. 2022, in preparation).

The second special target group are Kepler satellite field giants drawn from those studied by Takeda & Tajitsu (2017) and Singh et al. (2019a, 2021). These are identified in Table 1 by their Kepler Input Catalog (KIC) numbers. The Kepler-field giants have detailed evolutionary state information obtained through asteroseismology. We have observed 13 of these stars, but our selection was heavily biased toward those with known very high Li abundances. We are now gathering λ10830 observations for a much larger Kepler giant sample. Therefore we have chosen to report here the He measurements already done but will defer discussion on them until a larger set of spectra is gathered (A. Mallick et al. 2022, in preparation).

3. Observations and Reductions

We gathered HET/HPF high−resolution *zyJ* (8100−12750 Å) spectra of the program stars for about a year beginning in 2021 April. HPF was designed to aid in the search for low-mass companions to M-dwarf stars, and it has unique design features that deliver extremely high-precision radial velocities (down to $\sim$1–2 m s^{-1}). This instrument has been described in detail by Mahadevan et al. (2012, 2014).[17] HPF was configured for our program to deliver a spectral resolving power of $R \equiv \lambda/\Delta\lambda \sim 55{,}000$.

In the *zyJ* spectral region, telluric molecular blockage ranges from near zero to almost a complete blanket, varying significantly with wavelength. The dominant telluric contaminators are the H_2O bands, and their spectrum blockage can change substantially on timescales of hours to nights. Regular observations are obtained of rapidly rotating hot stars that can be used to cancel the telluric features in the program stars. The HET's fixed altitude is an asset here: all stars have identical air masses; thus it is not necessary to gather hot-star spectra to accompany each target spectrum. Divisor-star spectra adequate for our needs are normally gathered 1–2 times during nights with stable atmospheric conditions.

HPF observations of target and telluric divisor stars were initially reduced with the HPF pipeline code *Goldilocks*.[18] This facility, run automatically within a day of data acquisition, processes raw HPF data frames into useful spectra by removing bias noise, correcting for instrumental nonlinearity, masking significant anomalous radiation events, calculating the slope/flux and variance image using the algorithms from the *pyhxrg* module in the tool *HxRGproc* (Ninan et al. 2018), and performing optimal extraction of the 28 spectral orders. HPF's wavelength scale in spectra reduced with *Goldilocks* is extremely stable and accurate to levels far beyond those needed for our analyses of the program star spectra. For each stellar source, the *Goldilocks* spectral files have several extensions, including ones for the target, local night sky emission, noise, and wavelength calibrations.

The rest of the reductions were performed with the IRAF[19] (Tody 1986, 1993) facility. We used the *disptrans* task to shift the *Goldilocks* vacuum wavelengths to air wavelengths. Sky subtraction and mating of target fluxes and wavelengths produced standard echelle FITS spectra. We then performed continuum normalization of the target spectra and hot-star spectra via the *continuum* task and used the *telluric* task interactively to divide out this contamination from the target spectrum. Figure 2 illustrates the large number of telluric features in the HPF spectral order containing λ10830 and the necessity of iterative division operations to produce optimal elimination of the tellurics. A final continuum normalization was followed by merging into a single continuous spectrum with the *scombine* task.

To correct the observed stellar velocities to a rest wavelength scale accurate enough for our purposes, we first determined the velocity shifts using IRAF *splot* to measure the observed wavelengths of several strong atomic lines in the spectral order containing the He I λ10830 feature. Their average displacement from rest in velocity units provided a shift to the stellar rest velocity accurate to $\sim\pm$0.1 km s^{-1}.

In Figure 3 we display spectra of some typical program stars in the HPF order that contains the He I λ10830 feature. The left-hand panel shows essentially the entire order, covering the spectral range $\sim$10820−10960 Å. Star TYC 3590-03350-1 is at the low-temperature end, and TYC 0188-00998-1 is at the high-temperature end of our sample. Star TYC 1158-00345-1 has one of the larger Li abundances, log ϵ(Li) = 3.1 (Kumar et al. 2011 and references therein). TYC 4977-01458-1 and TYC-0188-00998-1 have high rotational velocities, and they have strong He I absorption lines, common among our program stars. The right-hand panel shows just a small wavelength interval centered on the λ10830 line.

4. He I λ10830 Analysis

Red giants present rich absorption-line spectra in the *zyJ* spectral domain. However, the present purpose is to investigate just the He I λ10830 transition. This line in absorption connects

[16] https://webda.physics.muni.cz/navigation.html
[17] See https://hpf.psu.edu/ for additional instrument information.
[18] https://github.com/grzeimann/Goldilocks_Documentation
[19] http://iraf.noao.edu/

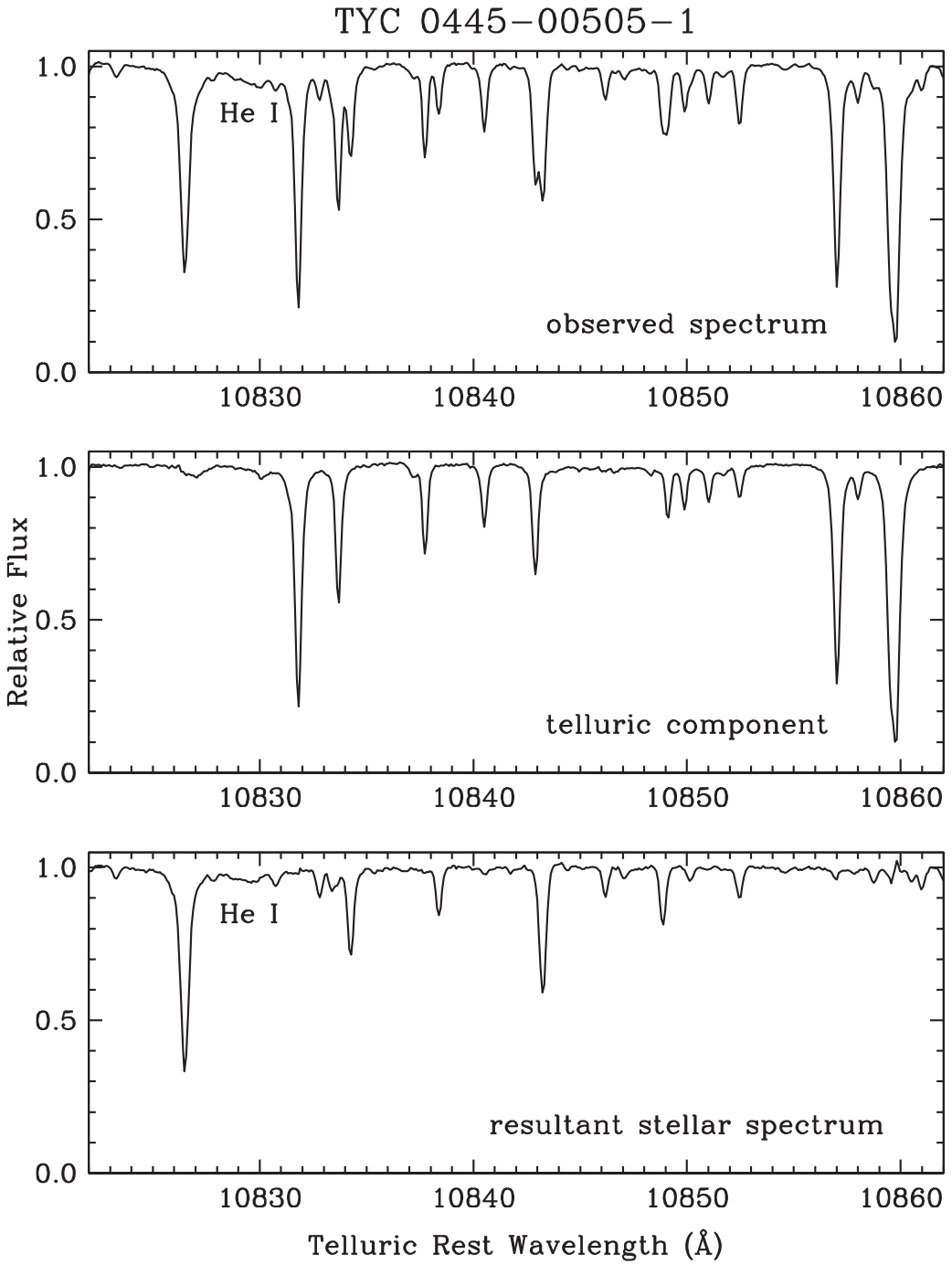

Figure 2. Example of telluric-absorption-line cancellation near the λ10830 transition. For this figure a program star with very high SNR but weak He I absorption depth was chosen. The top panel contains the stellar+telluric spectrum, and the middle panel has the spectrum of a warm (essentially featureless) star. The division of these two spectra produces the purely stellar program star spectrum in the bottom panel.

the energy states $1s2s^3S$ (19.82 eV) and $1s2p^3P^o$ (20.96 eV), as illustrated in Figure 3 of Preston et al. (2022). Neither the lower nor the upper state has a permitted transition to the $1s^2\ ^2S$ ground state. It is a hyperfine-split triplet, with components at 10829.09, 10830.25, and 10830.34 Å, with transition probabilities −0.745, −0.268, and −0.046, respectively, in the NIST database (Kramida 2019; Kramida et al. 2019).[20]

Appearance of the very-high-excitation He I λ10830 line in cool red giants essentially signals chromospheric activity that is detached from the formation of the photospheric spectrum. Its line profile can be very broad, in some cases covering several Ångstroms. In this small region there are several photospheric absorption lines, including the very strong Si I 10827.1 Å transition and other weak but detectable ones: Ti I 10827.9 Å, Ca I 10829.3 Å, and a couple of significant CN lines. In particular the Ca I line can significantly contaminate the He I transition. We wanted to make accurate estimates of the equivalent width (EW) of only the λ10830 He I feature, and so

[20] National Institute of Standards and Technology Atomic Spectra Database: https://www.nist.gov/pml/atomic-spectra-database.

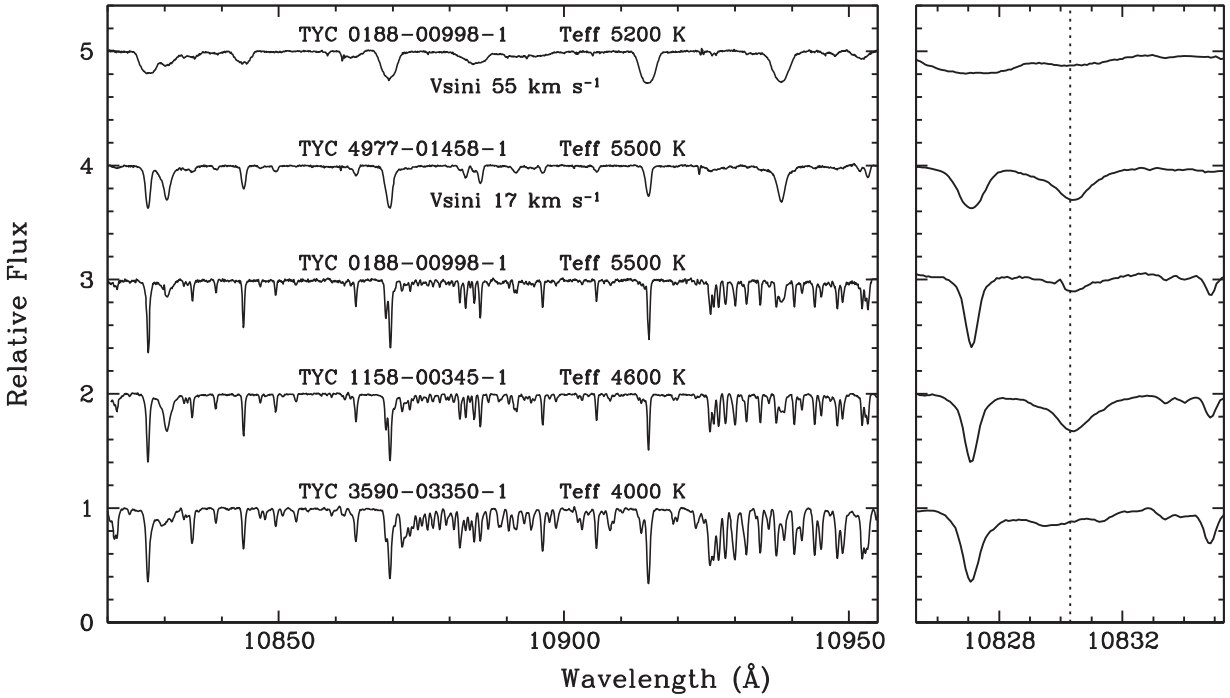

Figure 3. Reduced and telluric-corrected spectra of seven program stars in the HPF spectral order that contains He I 10830.3 Å. The left-hand panel shows the entire HPF order that contains the λ10830 line. The right-hand panel zooms in to a 10 Å interval centered on the λ10830 feature. The wavelength of the strongest two components of the He I triplet is shown with a dotted line.

we created synthetic spectra to match and then cancel the surrounding photospheric atomic and molecular transitions.

4.1. Line List for Synthetic Spectra

To generate line lists for the synthetic spectra, we used the *linemake* facility (Placco et al. 2021),[21] which begins with the Kurucz (2011, 2018)[22] line compendium and substitutes or adds line transition data generated in recent laboratory studies mainly by the Wisconsin–Madison atomic physics group (Den Hartog et al. 2021 and references therein) and by the Old Dominion University molecular physics group (e.g., Brooke et al. 2016 and references therein). Unfortunately there have been few laboratory atomic studies on transitions in the past couple of decades for the lines of interest near 10830 Å. Therefore we adopted the transition probabilities available in the NIST database for lines of the most prominent species in this spectral region: Na I, Mg I, Al I, Ca I, Fe I, and Sr II.

We tested this line list by generating synthetic spectra of the red giant standard star Arcturus. The observed spectrum was from Hinkle & Wallace (2005). We adopted the model atmosphere parameters derived by Ramírez & Allende Prieto (2011): $T_{\rm eff}=$ 4286 K, $\log(g)=1.66$, $[{\rm Fe/H}]=-0.52$, $V_{\rm mic}=1.74\,{\rm km\,s^{-1}}$, as well as the elemental abundance ratios given in that paper. We produced an interpolated model with these values from the Kurucz (2011, 2018) grid[23] using software developed by A. McWilliam & I. Ivans (2022, private communication). The synthetic spectra for Arcturus and all other stars in this paper were generated using the current version of the LTE synthetic spectrum code MOOG (Sneden 1973).[24]

Iterative comparison of observed and synthetic Arcturus spectra led to adjustments in the transition probabilities and wavelengths of some transitions in the line list. In making these changes we did not alter any atomic or molecular line data that were from NIST or recent laboratory analyses. Finally, to verify the reasonableness of the final line list we also checked its applicability to the spectra of the Sun and a couple of program stars. This procedure yielded an atomic/molecular line list for our task of adequately matching synthetic and observed photospheric spectra of our red giant stars, but should not be confused with a list that would be appropriate for detailed abundance analyses.

4.2. Estimated Model Photospheres

Nearly all of our program stars are Galactic disk red giants, having metallicities almost entirely in the domain $[{\rm Fe/H}]\gtrsim -0.5$. With the goal limited to adequate removal of the photospheric spectrum near the He I λ10830 feature, we adopted effective temperatures $T_{\rm eff}$ from photometry and surface gravities $\log(g)$ representative of first-ascent, RC, and RHB giants at the chosen $T_{\rm eff}$ values.

We first constructed a set of model stellar photospheres. The desired parameter domain can be seen both in a color–magnitude diagram (CMD) and a $T_{\rm eff}-\log(g)$ HR diagram of our targets. From the magnitudes and parallaxes in Table 1, and ignoring possible interstellar reddening corrections,[25] we constructed the CMD shown in the top panel of Figure 4. Added to this figure is a shaded area that approximately outlines the red horizontal-branch CMD area identified empirically by Kaempf et al. (2005) in M_V versus $B-V$ coordinates. In this figure

[21] https://github.com/vmplacco/linemake
[22] http://kurucz.harvard.edu/linelists.html
[23] http://kurucz.harvard.edu/grids.html
[24] Available at http://www.as.utexas.edu/~chris/moog.html.

[25] Most of our stars are bright and have distances <1 kpc, so the reddening should usually be small. Moreover, we lack the information to assess reddening corrections accurately for most of our targets.

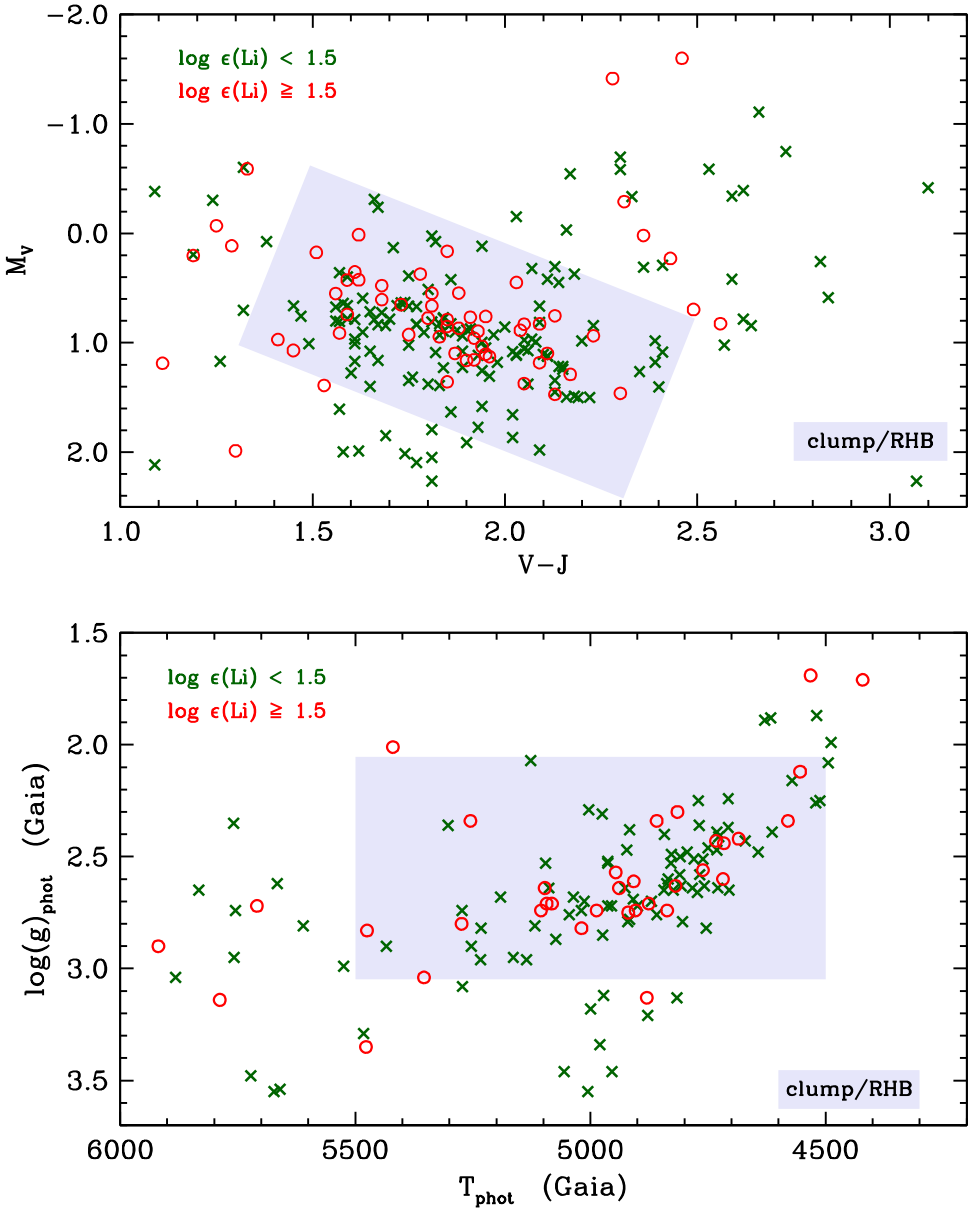

Figure 4. Top panel: color–magnitude diagram (CMD) for the targets. The plot boundaries have been set to show only the CMD area containing the first-ascent red giants, the RC, and the RHB. The main sequence, most of the subgiant branch, and the luminous giants and supergiants are outside of this CM area. Different colors and symbols denote Li-rich and Li-poor stars, and a freehand shaded region represents the He-fusing RC/RHB domain. Bottom panel: HR diagram based on Gaia photometric quantities. The colors and symbols are the same as in the top panel.

panel the majority of our stars have CMD locations consistent with RC/RHB membership, and there is no apparent segregation between Li-rich and Li-poor stars. On average they occupy the same evolutionary states.

In the bottom panel of Figure 4 we plot the $T_{\rm eff}$ and $\log(g)$ values of the program stars estimated from Gaia early data release 3 (EDR3; Gaia Collaboration et al. 2020) photometry. Here the shaded area represents the RC/RHB $T_{\rm eff}$ domain used by Afŝar et al. (2018). There are fewer data points in this Figure 4 panel than in the top one simply because many program stars do not have Gaia $T_{\rm phot}$ and $\log(g)_{\rm phot}$ values. However, inspection of both upper and lower panels suggests the same conclusion: most stars reside in the RC/RHB region, and on average the locations of Li-poor and Li-rich stars are the same.

We extracted model atmospheres from the ATLAS grid (Kurucz 2011, 2018). The model effective temperatures were computed in steps of 100 K in the range $4000 \leqslant T_{\rm eff} \leqslant 5600$ K. The model gravities were estimated from recent empirical temperature–gravity correlations for metal-rich giant stars: Figure 8 of Afŝar et al. (2018) and Figure 3 of Casey et al. (2019). At the high-temperature end nearly all stars are on the core helium-burning horizontal branch, so we adopted a uniform $\log(g) = 3.0$ in the range 5300−5600 K. For cooler temperatures the adopted gravities were decreased steadily, ending with $\log(g) = 1.3$ at $T_{\rm eff} = 4000$ K. Model metallicities were assumed to be solar, $[{\rm M/H}] = 0.0$, and microturbulent velocities were assumed to be $V_{\rm mic} = 2.0\,{\rm km\,s^{-1}}$; neither of these model parameter choices were critical for our desired photospheric spectrum computations.

Whenever possible, we used observed $V - J$ colors and the color–$T_{\rm eff}$ relations of Ramírez & Meléndez (2005) to select appropriate $T_{\rm eff}$ values for each star, adopting a model

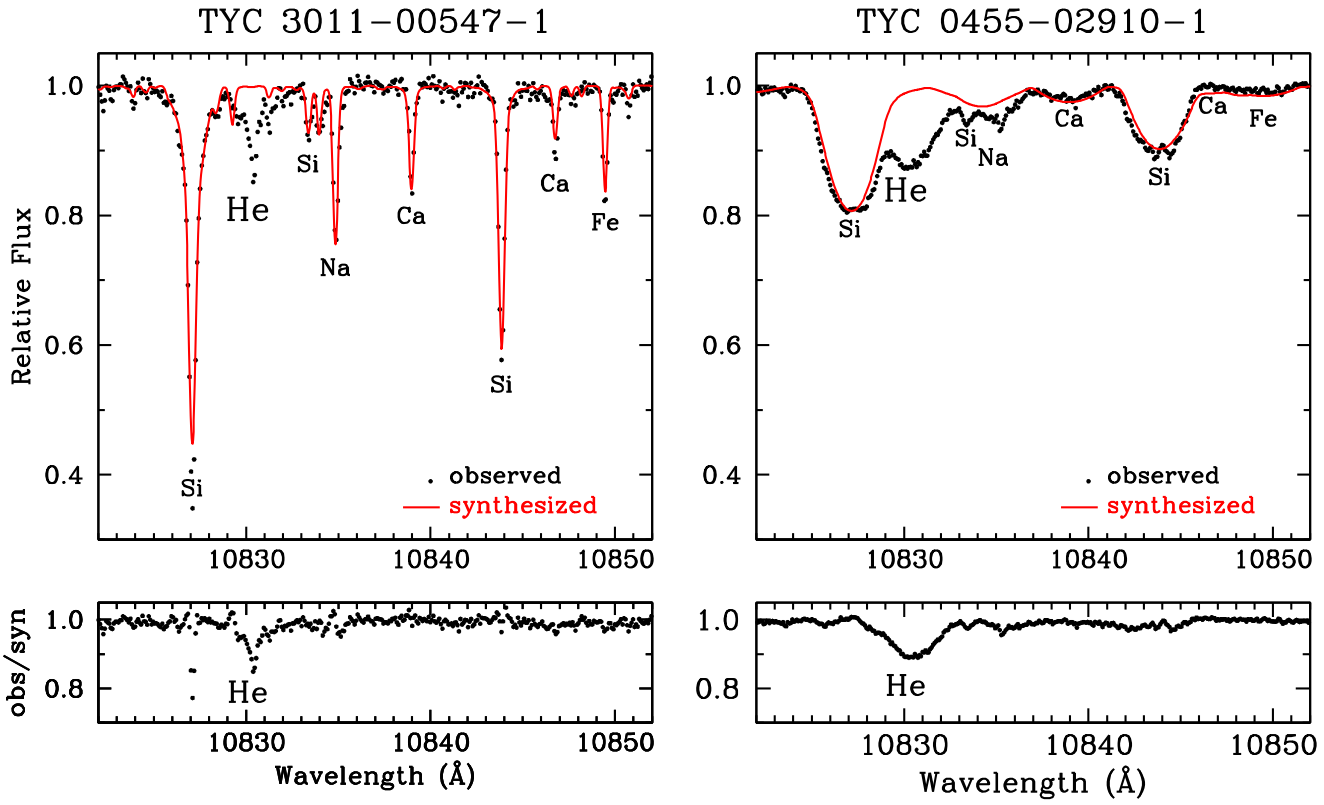

Figure 5. Examples of photospheric spectrum cancellation. For each star the top panel shows an observed spectrum (black points) and the best-fit model photospheric spectrum (line), and the bottom panel shows the result of the observed/computed division.

atmosphere with the parameters as described above. When J magnitudes were not available we used $B-V$ colors, and in a handful of cases we adopted models near those derived in individual papers, or simply guessed at a starting model parameter set. In this procedure we ignored possible interstellar reddening because our stars are mostly near enough to not suffer large amounts of extinction, as noted above. We reemphasize that we used the modeling only to reasonably match the photospheric spectrum transitions. Our procedures were entirely inadequate for detailed photospheric analyses, and so we do not publish the model parameters adopted here.

4.3. Observed/Synthetic Spectrum Matches

We computed synthetic spectra of the stars in the 10820−10960 Å region (the complete HPF spectral order containing λ10830), using the line list described in Section 4.1 and model atmospheres in Section 4.2. The computed synthetic spectra were compared interactively with the observed spectra. The syntheses included combined thermal, microturbulent, and collisional damping line broadening effects, while the observed lines included these and additional broadening due to instrumental, macroturbulent, and in some instances rotational effects. These extra broadening contributions were accounted for in most cases by Gaussian smoothing functions with empirically determined broadening values that minimized the differences between the observed and synthetic spectra. From iterative spectrum matches we were able to determine Gaussian FWHM values to precisions of $\sim\pm0.02$ Å. For some stars the smoothing functions combined Gaussian and rotational factors. In Section 4.5 we discuss the spectrum line broadening in more detail.

We then performed a rough abundance determination in order to best match the synthetic and observed spectra near 10830 Å. We began with setting the N abundance, because the CN (0−0) Q-branch bandhead culminating at 10925 Å and the (0−0) R-branch bandhead at 10870 Å often dominate those spectral regions (see Figure 3), and weaker CN lines occur in the whole spectral order. Then we altered the Fe, Si, and Ca abundances to minimize the differences between the synthetic and observed atomic lines. Although Na I, Ti I, and Sr II have significant absorption lines in this spectral order, none of them are close enough to the He I λ10830 transition to matter for our work.

The final step was to divide the stellar and synthetic photospheric spectra to yield an essentially pure chromospheric spectrum of the He I line. In Figure 5 we show examples of the He I isolation and measurement process for a typical program star with a modest He I line, and for a rapid rotator with a much stronger line. For the left-hand panels, TYC 3011-00547-1 was chosen to illustrate typical SNR conditions and the limits to our ability to completely extinguish the photospheric spectra. In the right-hand panels we show the same observed, synthetic, and resultant spectra for the rapidly rotating star TYC 0455-02910-1. Contamination by neighboring photospheric features is the dominant uncertainty source here. However, the λ10830 line clearly is strong in the divided spectrum.

4.4. Equivalent Widths

We measured the EWs of the λ10830 lines using the specialized spectrum analysis code SPECTRE (Fitzpatrick & Sneden 1987).[26] The He I transition is usually very broad, with

[26] Available at http://www.as.utexas.edu/~chris/spectre.html.

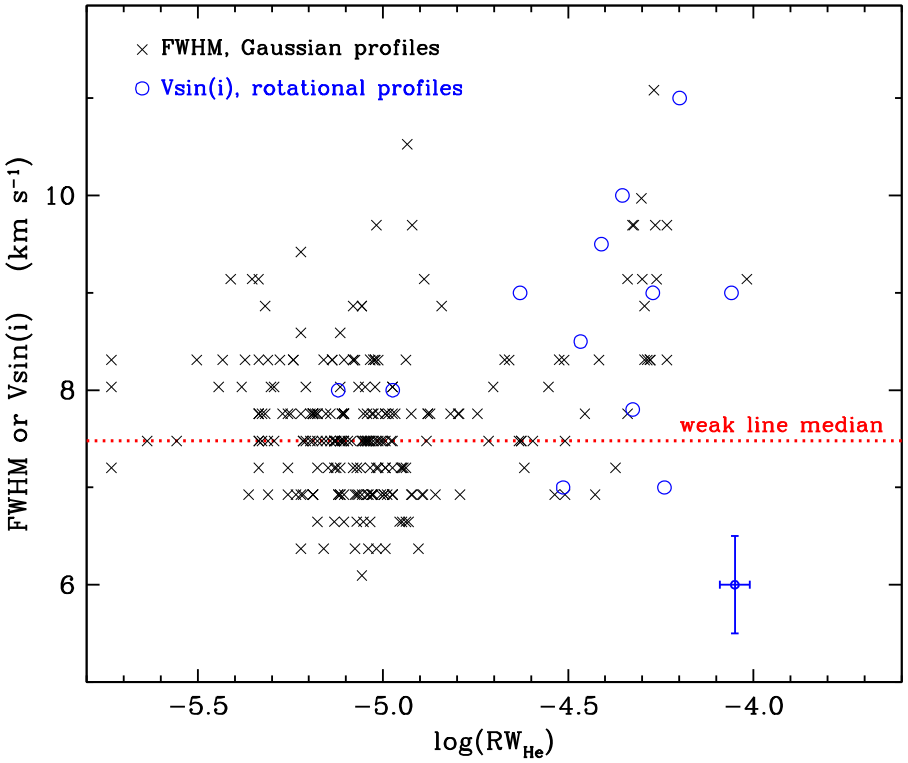

Figure 6. Empirical broadening estimates compared to He I λ10830 reduced widths for stars that have relatively narrow line profiles. Point, line, and color types are identified in the figure. The ordinate of the plot is restricted to 0−12 km s^{-1} in order to see individual points clearly. This means that stars with $V\sin(i) \gtrsim 12$ km s^{-1} are not shown here. The point with error bars in the lower right-hand corner represents the typical uncertainties of the measurements, as explained in the text. The FWHM values were estimated to the nearest 0.01 Å ($\simeq$0.3 km s^{-1}), as can be seen in their "quantized" values.

extended wings sometimes covering more than 2 Å. Its line profile often has small distortions due to incomplete cancellation of telluric and photospheric contaminating features. Therefore we measured EW_{He} via direct Simpson's rule[27] integrations. The EW_{He} values are listed in Table 1.

He I absorption is always present in our stellar sample, albeit very weak and hard to measure in a few stars. There is a very large star-to-star λ10830 equivalent width range, $EW_{He} \simeq$ 20−1300 mÅ. Therefore for the remainder of this paper we will quote reduced widths for the 10830 Å lines:

$$\log(RW_{He}) \equiv \log_{10}(EW_{He}/\lambda) = \log_{10}(EW_{He}/10830), \quad (1)$$

where EW_{He} is in units of Å. The $\log(RW_{He})$ range in our stars is $\simeq$−5.7 to −3.6.

For TYC 3011-00547-1 (Figure 5 left panels) we measured $\log(RW_{He}) = -4.94 \pm 0.04$ (EW = 125 ± 13 mÅ), with the large uncertainty value based mostly on continuum placement, which directly impacts the wavelength extent of the He I line wings. For TYC 0455-02910-1 (Figure 5 right panels) we found $\log(RW_{He}) = -4.50 \pm 0.03$ (EW = 345 ± 15 mÅ). Our measurements of λ10830 in the full sample yielded an estimated general $\log(RW_{He})$ uncertainty of ±0.04 dex, which we will adopt hereafter in this paper.

4.5. Line Broadening

As described in Section 4.3, for spectra without detectable rotational line broadening we used comparisons of observed and synthetic spectra to estimate FWHM values for the Gaussian smoothing functions that account for instrumental and macroturbulent broadening. In Figure 6 we correlate these FWHM estimates with He I reduced widths. The ordinate of this figure covers only the line breadth range $5 < \text{FWHM} < 12$ km s^{-1}, allowing one to see that our FWHM estimates were quantized. That is, in the synthesis/observation comparison, the FWHM values were changed in steps of 0.01 Å, which translates to the spacing of $\simeq$0.28 km s^{-1} that can be seen in Figure 6. For stars with quiet chromospheres, $\log(RW_{He}) \lesssim -4.8$, the observed photospheric-line widths appear to be constant to within our measurement uncertainties. Neglecting the few aberrant points with FWHM $\gtrsim$ 9 km s^{-1}, the mean value is $\langle\text{FWHM}\rangle = 0.28$ Å (σ = 0.03 Å), or 7.7 km s^{-1} (σ = 0.5 km s^{-1}). The median value is slightly lower: 7.5 km s^{-1}, which is indicated by the dotted red line in Figure 6.

The instrumental resolving power $R = 55{,}000$ contributes 5.5 km s^{-1} to the FWHM. We cannot determine directly a macroturbulent velocity, but the comparison between observed and instrumental FWHM values suggests that $V_{mac} \simeq 2.2$ km s^{-1}, a number that is nearly identical to our assumed $V_{mic} = 2.0$ km s^{-1}. If $V_{mac} \sim V_{mic}$, then the empirically measured Gaussian smoothing values for stars with weak λ10830 lines appear to successfully account for realistic line broadening in our red giants. We adopt 0.5 km s^{-1} as a reasonable estimate of the FWHM uncertainties derived from our simple estimates.

In Figure 6 some stars are identified as rapidly rotating, meaning that our synthetic-observed spectrum matches were improved by applying a combination of rotational and Gaussian smoothing to the calculated syntheses. Our rotational line

[27] See, e.g., https://math24.net/simpsons-rule.html.

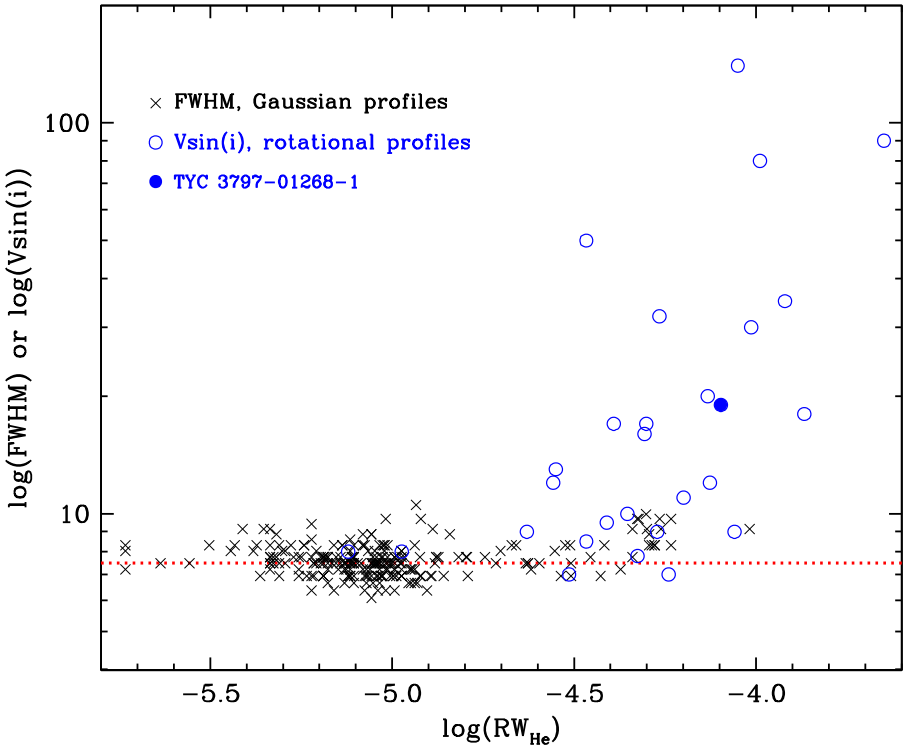

Figure 7. Empirical broadening estimates compared to He I λ10830 reduced widths for the whole sample. Point types and colors are as in Figure 6, except that a filled circle is used to call attention of TYC 3797-01268-1, a program star with large infrared color excesses. This object will be discussed in Section 5.3.

broadening estimates were entirely empirical, based on standard relations,[28] with an assumed limb darkening coefficient $u = 0.5$ (see Figure 17.6 in Gray 2008). We found through repeated trials on many program star spectra that rotation could only be detected with confidence at smoothing widths $\gtrsim$10 km s^{-1}. In the cases for which rotation could be detected, we set the Gaussian components (accounting for all broadening sources except rotation) to have FWHM values of 0.25 km s^{-1}. The rest of the broadening was assumed to be caused by rotation. In Figure 6 the widths plotted for these stars are the rotational Vsin(i) values only.

There were some stars with derived FWHM $\gtrsim$ 10 km s^{-1} for which we could not detect rotational broadening with certainty. In these cases we have reported Gaussian-only broadening. It is likely that in some cases such stars have rotational signatures that will be revealed with more rigorous analyses of spectra covering a much larger wavelength range than that studied here. The Gaussian or rotational broadening values for all stars are listed in Table 1.

In Figure 7 we plot log(RW$_{\rm He}$) versus the FWHM for all of the program stars. Red giants with large λ10830 absorption features can have sharp line profiles (FWHM < 10 km s^{-1}) or can have obvious rotationally broadened spectra. However, nearly all of our rapidly rotating program stars have very strong He I absorption features (log(RW$_{\rm He}$) $\gtrsim -4.7$). There are only two exceptions in our sample.

We have searched the literature for published Vsin(i) measurements of our stars. Various papers have used heterogeneous methods to derive Vsin(i) from spectroscopic data sets with a variety of attributes. In Table 2 we list these literature values and their sources. Figure 8 shows a comparison of our rotational velocity estimates with the published ones, and from the statistics quoted in the figure legend, it is clear that they are in good agreement. Note the small systematic offset at the low Vsin(i) end of the correlation. This indicates that translation of our measured line widths into Vsin(i) values is probably too simplistic for the complex combination of instrumental, thermal, microturbulent, macroturbulent, and rotational line components at small rotational velocities.

Table 2
Rotation Rates: This Study and Literature

Star	Vsin(i)[a] (km s^{-1})	Vsin(i)[b] (km s^{-1})	Source
TYC 0347-00762-1	18.0	15.3	Bizyaev et al. (2010)
TYC 0429-02097-1	12.0	11.3	Yan et al. (2018)
TYC 0455-02910-1	50.0	58	Lyubimkov et al. (2012)
TYC 0575-00918-1	35.0	42	Kriskovics et al. (2014)
TYC 1005-00073-1	80.0	84.1	Massarotti et al. (2008)
TYC 1395-02327-1	90.0	90	Uesugi & Fukuda (1970)
TYC 2120-00320-1	32.0	28.7	Takeda & Tajitsu (2017)
TYC 2527-02031-1	7.8	6.1	Rebull et al. (2015)
TYC 2724-02354-1	140.0	139.7	Massarotti et al. (2008)
TYC 3134-00265-1	12.0	13.09	Ceillier et al. (2017)
TYC 3282-02270-1	9.0	7.2	Gonćalves et al. (2020)
TYC 3318-00020-1	17.0	16.3	Adamów et al. (2014)
TYC 3340-01195-1	9.5	8.4	Rebull et al. (2015)
TYC 3590-03350-1	8.5	6.4	De Medeiros et al. (2002)
TYC 3676-02387-1	11.0	11.8	Adamów et al. (2014)
TYC 3797-01268-1	19.0	17.6	Balachandran et al. (2000)
TYC 4222-01254-1	30.0	22.1	Guillout et al. (2009)
TYC 4977-01458-1	17.0	15.5	Massarotti et al. (2008)

Notes.
[a] This study.
[b] Literature.

[28] e.g., http://www.astro.uvic.ca/~tatum/stellatm/atm6.pdf.

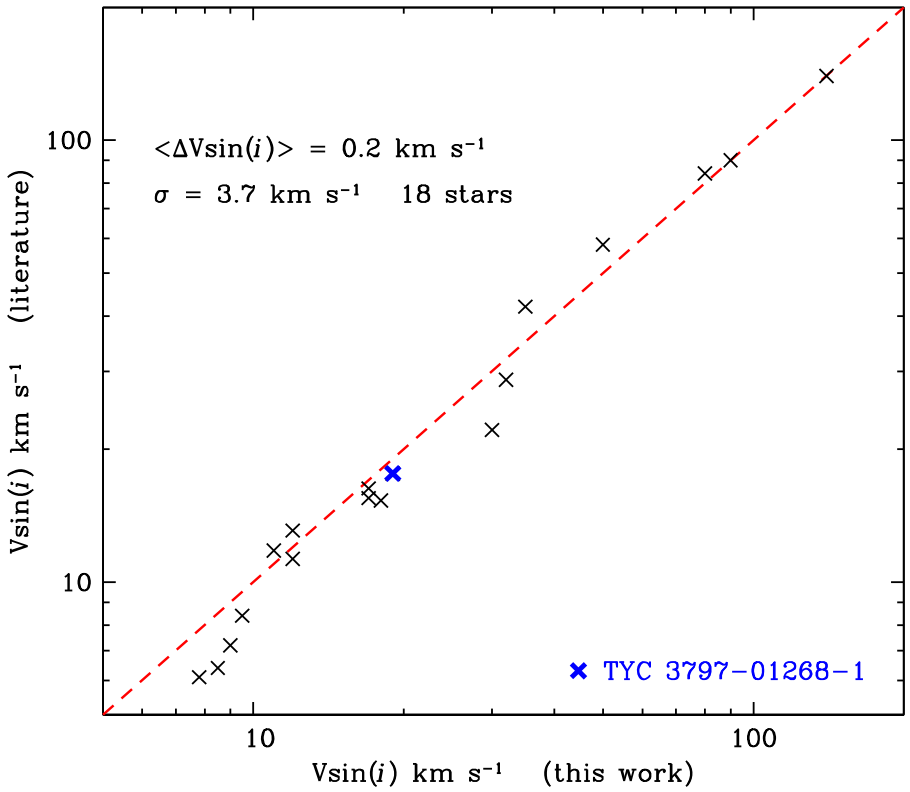

Figure 8. Comparison of *V*sin(*i*) estimates in this work vs. values published in various literature sources. The red dashed line indicates agreement between the two data sets. The thick blue × symbol marks TYC-3797-01268-1, noted earlier in Figure 7.

5. Li and He in Li-poor and Li-rich Stars

Our basic result is that strong He I λ10830 absorption is rare in Li-poor stars but very common in Li-rich ones. This conclusion is clear in Figure 9, where we compare Li abundances and log(RW_{He}) values, and in Figure 10, where histograms of log(RW_{He}) are shown for the Li-poor and Li-rich groups. The horizontal shaded area centered at $\log \epsilon(\mathrm{Li}) = 1.25$ divides the Li-poor and Li-rich abundance regimes, and the vertical band at $\log(RW_{He}) = -4.85$ divides the weak and strong He I absorptions. These lines create four apparent quadrants of different Li abundances and He strengths, as labeled in the figure. These group separations were determined empirically, and they merit further discussion.

In this exercise one should keep in mind that our stellar sample is not statistically robust. First and foremost, all of our Li abundances are literature values, which guarantees their heterogeneity. We have made no attempt to put them on a common abundance system with consistent atmospheric parameters. This is of no consequence for stars with very large Li abundances. However for stars with lesser abundance values, $1.0 \lesssim \log \epsilon(\mathrm{Li}) \lesssim 1.5$, assignments into Li-rich or Li-poor categories should be viewed with caution. Second, our Li-rich stars were chosen through a literature search for reports of such stars. Some of the papers considered the relative frequency of Li-rich stars, and others concentrated mostly on the properties of individual Li-rich objects. Our Li-rich stars have irregular literature histories.

5.1. Li-poor Stars with Weak He I λ10830 Absorptions

For the Li-poor stars we used mostly candidates from the surveys of Adamów et al. (2014) and Afşar et al. (2018), neither of which were biased in any way on Li abundances. The Adamów et al. sample was the set of red giants of the Penn State-Toruń Planet Search (PTPS) program (Deka-Szymankiewicz et al. 2018 and references therein). Their Li abundances were derived in that paper and thus took no part in sample selection. The Afşar et al. target list was formed from CMD searches for stars that appeared to be in the He-burning red horizontal-branch domain, ignoring possible Li abundance information. The Li abundances for these stars in Table 1 will be presented by Z. Bozkurt et al. (2022, in preparation). In general, our Li-poor stars have an abundance spread that is typical for normal red giants.

The observed distribution of log(RW_{He}) among Li-poor stars in the lower left quadrant of Figure 9 shows a sharp drop in number near $\log(RW_{He}) \simeq -4.85$, with an uncertainty of about ±0.05 by visual inspection. We have 187 Li-poor stars as defined earlier ($\log \epsilon(\mathrm{Li}) < 1.5$). Of these, 168 stars have log (RW_{He}) < −4.85, or 90%, while only 18 (10%) have stronger λ10830 He I absorptions. Small alterations of the Li abundance and He line strength dividing lines would do quantitatively little to this result. The vast majority of red giants have small Li abundances and weak He I λ10830 transitions. For the rest of this paper we adopt $\log(RW_{He}) = -4.85$ as the estimated break point between stars with weak and strong λ10830 transitions.

With this He I estimated strength boundary we revisit the CMD of Figure 4, and in Figure 11 we show the M_V versus $V-J$ diagram with points separated at $\log(RW_{He}) = -4.85$. Comparison of this figure to the top panel of Figure 4 reveals general similarity. The majority of both He-weak and He-strong stars reside in the clump/RHB domain, and there is no obvious separation between the CMD distributions of the two He groups. Strong He I absorption features, like large Li

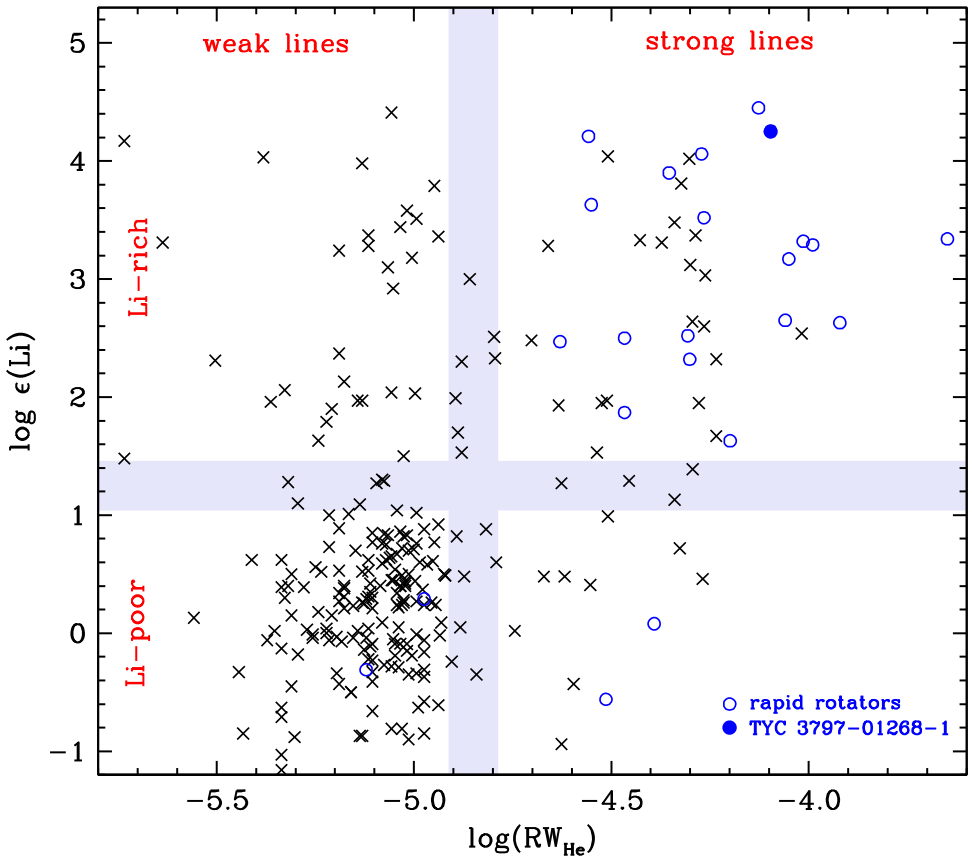

Figure 9. log(RW$_{He}$) values vs. lithium abundances log ϵ(Li). The horizontal shaded region serves to roughly divide Li-rich from Li-poor stars, and the vertical shaded region separates the weak and strong λ10830 absorption strengths. The location of these lines is discussed in the text. As in Figures 6 and 7, black × symbols represent stars with Gaussian measured line profiles, blue open circles are stars with rotational line profiles, and a blue filled circle denotes TYC 3797-01268-1 (see Section 5.3).

abundances, appear most frequently in red giant clump and red horizontal-branch stars.

Investigation of He absorption in red giants began with the moderate resolution ($R \sim 14{,}000$) image-tube survey by Zirin (1982) of 455 stars of interest identified from Ca II K-line measurements, and X-ray, and variability studies. O'Brien & Lambert (1986) provided the pioneering high-resolution ($R \simeq 54{,}000$), high SNR (typically $\gtrsim$100) survey of λ10830 for G–K–M giants and supergiants. Many of their targets were either luminous giants and supergiants (luminosity classes I–II) or very cool ones (temperature class M). Such stars often have large and variable He I λ10830 profiles, usually dissimilar to those in the G–K giants of interest here. However, O'Brien & Lambert identified a class of less luminous K giants, which they labeled "β Gem type," that have relatively modest λ10830 absorptions, which do not appear to vary much with time. With the $(V-J)$ and M_V values constructed from SIMBAD (Wenger et al. 2000) data, we identified about 25 of their stars lying within the boundaries of Figure 4. A direct comparison of their EW values with our measurements is not possible because their sample has only very bright stars ($J < 3.0$) that cannot be observed with HET/HPF. However, we estimated a median log (RW$_{He}$) ~ -4.95 for their less luminous K giants, less than our estimated upper limit for weak λ10830 lines. The median for our Li-poor stars, log(RW$_{He}$) ~ -5.10, is somewhat smaller than that from O'Brien & Lambert (1986), but with different instruments, different log(RW$_{He}$) measurement techniques, and lack of stars in common, this small issue will not be pursued further.

5.2. The Li-poor/Li-rich Split

Papers discussing Li abundances in red giants usually adopt log ϵ(Li) = 1.5 as the minimum abundance for a star to be considered as Li-rich, and we have followed this practice earlier in the paper. This value goes back to the Iben (1967) stellar evolutionary computations, leading to "a standard first dredge-up dilution factor of ∼60, for a star with an initial cosmic abundance of 3.3 dex." (Charbonnel et al. 2020). However, today we recognize that the actual distribution of Li in evolved stars is the result of a complex set of processes involving stars of different masses beginning with a variety of initial conditions, followed by Li destruction mechanisms throughout the main-sequence and subgiant evolutionary phases. Several recent papers consider this point, including Aguilera-Gómez et al. (2016), Casey et al. (2019), Charbonnel et al., Kumar & Reddy (2020), Deepak & Lambert (2021), and Martell et al. (2021). It is evident from these studies that Li enhancement is mostly associated with RC giants in the He-core-burning phase. Singh et al. (2021) proposed the reclassification of RC giants based on Li abundances and asteroseismic properties into three categories: Li-normal (log ϵ(Li) < 1.0), Li-rich (1.0 < log ϵ(Li) < 3.2), and super-Li-rich (log ϵ(Li) > 3.2). Thus the "traditional" Li-rich marker, log ϵ(Li) = 1.5−1.8 depending on the mass, is now recognized as a convenient

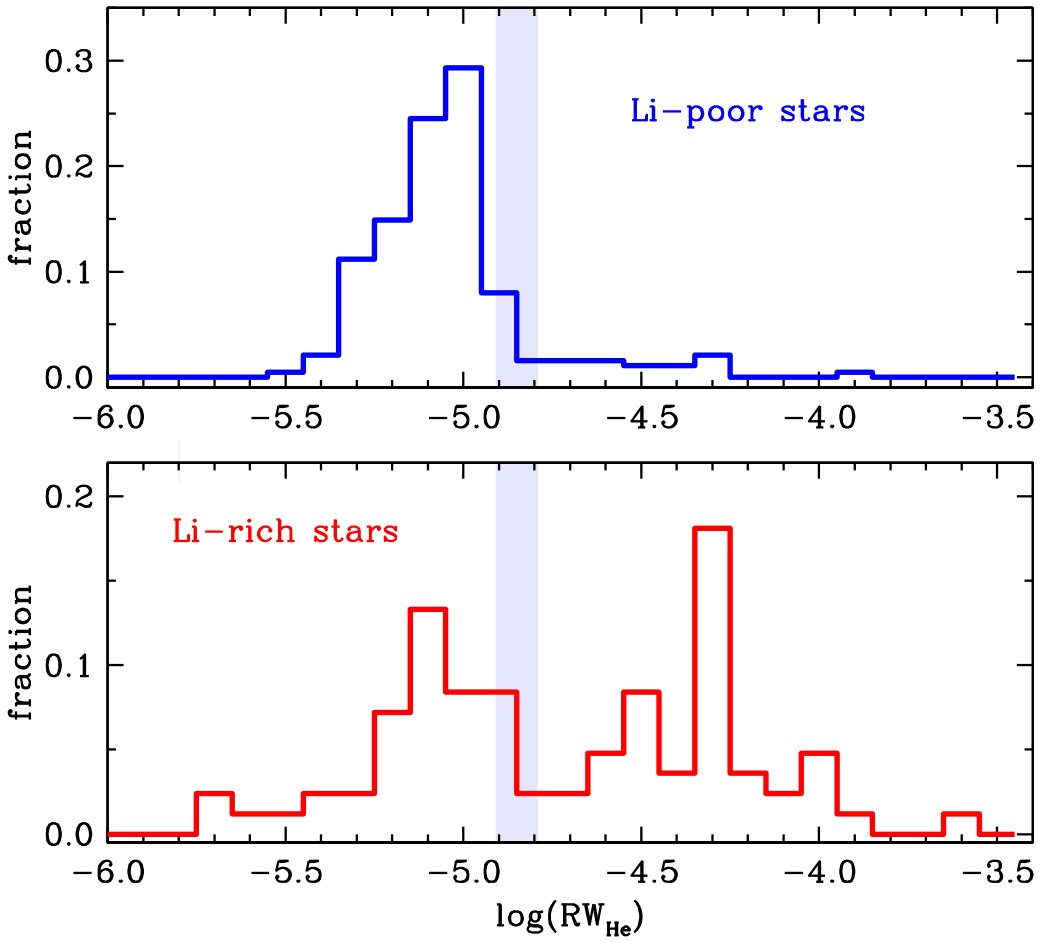

Figure 10. Histograms representing the distribution of log(RW$_{He}$) values for Li-poor (upper panel) and Li-rich (lower panel) stars. The vertical shaded region, drawn at log(RW$_{He}$) = −4.85 as in Figure 9, separates the weak and strong λ10830 absorption strengths.

upper limit for giants ascending the RGB for the first time but too simplistic in describing the Li abundance history of real stars. The only reported Li-rich first-ascent RGB giant that has been classified using asteroseismic data is KIC 9821622 (Jofré et al. 2015). Singh et al. (2020) have reanalyzed this star and derived a lower Li abundance, substantially smaller than the suggested super-Li-rich category. As of today we do not know of any giant with log ϵ(Li) > 1.8 that is classified as a giant ascending the RGB with a He-inert core based on asteroseismic analysis; certainly no super-Li-rich RGB giant has been found (Singh et al. 2019a).

Our assessment of the Li-poor/Li-rich division comes simply from inspection of the distribution of points in Figure 9. The most obvious separation of stars in Li abundance occurs near log ϵ(Li) ≃ 1.0, with Li-poor stars aggregating at small log (RW$_{He}$) values while Li-rich stars have much larger star-to-star log(RW$_{He}$) scatter. Therefore, we have chosen to set the Li-rich/Li-poor split at log ϵ(Li) = 1.25, with an uncertainty of at least 0.1 dex. We emphasize again that this line is a convenient demarcation between the two Li stellar groups, and it should not be considered a well-determined rigid boundary.

5.3. The Li-rich Red Giants

Our sample has 84 stars with log ϵ(Li) > 1.25. Of these, 46 have log(RW$_{He}$) > −4.85 (55%). This high fraction of Li-rich stars with strong λ10830 absorptions can be easily seen in Figure 9 and in the bottom panel of Figure 10. Small adjustments of the Li abundance and/or He I line strength divisions do not disturb the basic positive Li/He connection in Li-rich stars.

Almost all of the strongest λ10830 features are detected in rapidly rotating stars. Nine of the 10 stars with log (RW$_{He}$) > −4.2 (EW > 680 mÅ) have rotational metal line profiles. However, many Li-rich stars with −4.85 < log(RW$_{He}$) < −4.20 exhibit no excess line broadening. Therefore, in line with conclusions of literature Li-abundance studies, it is clear that rapid rotation is not a requirement for either Li-abundance excess or for strong He I absorption. It is more certain that rotation is linked to strong He I lines. Our sample has 28 stars with detectable rotational line profiles, and only 2 of them have weak λ10830 absorptions, log(RW$_{He}$) < −4.85 (Table 1).

Large rotation and strong λ10830 absorption do not guarantee large Li: three such stars in Figure 9 have log ϵ(Li) $\lesssim$ 0.0. However, Li enhancement among giants is a transient phenomenon; very large Li abundances decline with time, as shown by Singh et al. (2021). The consequence of this is that there may be some Li-poor giants that still have strong He I λ10830 transitions and high rotation rates.

The λ10830 triplet has become a powerful diagnostic of physical conditions and dynamics in many stellar and exoplanetary objects. As discussed in Section 4 the lower energy level of the transition lies at 19.8 eV and is metastable. This mandates that reasonably high chromospheric temperatures are required to produce the line; it cannot be a photospheric

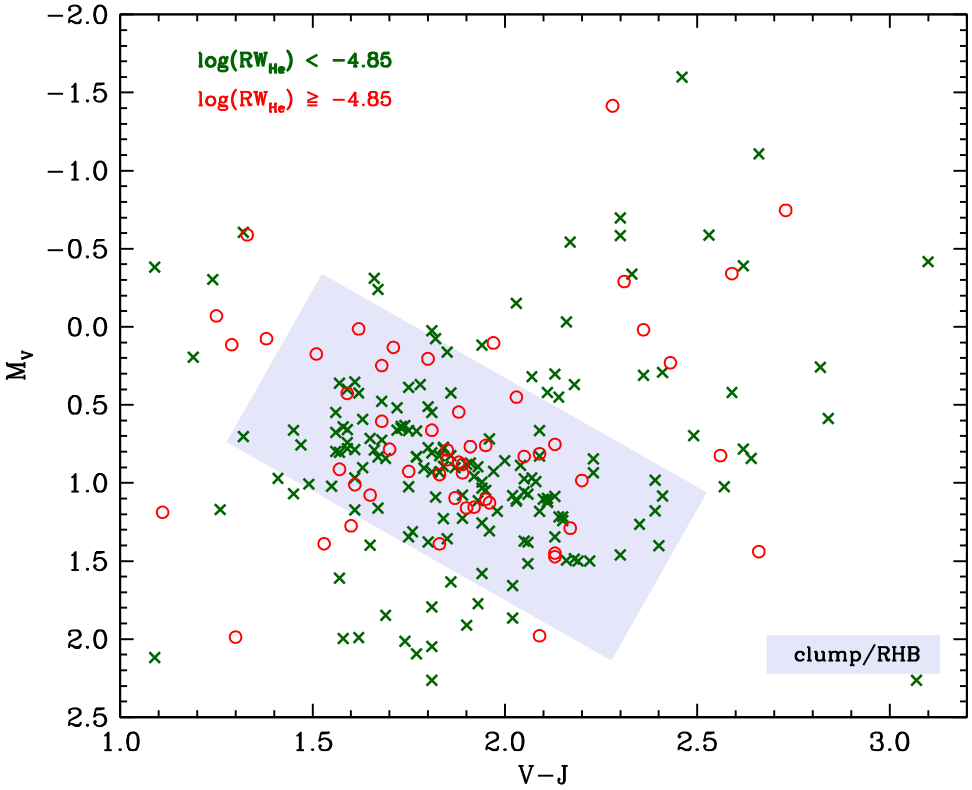

Figure 11. Another CMD for the targets. This plot contains the same data that are displayed in the top panel of Figure 4, but here the stars are divided into He-weak and He-strong groups, as indicated in the figure legend.

transition. Direct evidence from the Sun demonstrated that the transition could be produced as a result of photoionization by radiation occurring shorter than 504 Å, followed by recombination into the lower metastable level of the transition. The relationship between X-ray radiation and the strength of the helium line in the solar case (Harvey et al. 1975; Cranmer 2009) inspired early studies of the transition in cool stars (O'Brien & Lambert 1986; Zarro & Zirin 1986). These authors found a strong correlation between the EW of the λ10830 line and the value of L_X/L_{bol} for cool dwarfs and for G and K giant stars. Sparse data exist for G and K supergiants, but a correlation appears likely.

A direct measure of the photoionizing flux in dwarfs and giants suggested that the photoionization and recombination process dominates in giant stars. However, active dwarfs and subgiants appear not to exhibit a correlation between the photoionizing flux and helium line strength, presumably due to their higher chromospheric densities (Sanz-Forcada & Dupree 2008).

Another feature of the λ10830 transition derives from its metastable nature, which makes the line profile a tracer of a stellar wind flow. Dupree et al. (1996) detected blue-wing asymmetries of this transition, leading to the inference of radial outflows from the Sun. This feature has also been seen in luminous stars (O'Brien & Lambert 1986) including metal-poor field giants (Dupree et al. 1992, 1996). However, stellar winds are unlikely to be major contributors to the He I line formation in almost all of our stars. In Figure 12 we show a mean line profile for the 40 stars with strongest λ10830 absorptions ($\log(RW_{He}) > -4.85$) that either are without detectable rotation or are not rotating rapidly ($V\sin(i) < 10\,km\,s^{-1}$). The coadded spectra are those that have already undergone photospheric spectrum cancellation (Sections 4.3, 4.4). Inspection of the mean profile reveals the presence of the weakest of the λ10830 triplet members at 10829.09 Å, but otherwise it appears to have symmetric blue and red wings centered on the lab wavelength of the two main triplet members. There is no evidence for the blue asymmetries that are seen in some luminous stars of the papers cited above.

5.4. He I λ10830 in the Unusual Li-rich Star TYC 3797-01268-1

TYC 3797-01268-1 (HD 233517) has unique properties among our program stars. Fekel et al. (1996) first reported on the high lithium and rotation of this star. In Tables 1 and 2 we quote the Balachandran et al. (2000) values of $\log\epsilon(Li) = 4.2$ and $V\sin(i) = 17.6\,km\,s^{-1}$. Jorissen et al. (2020) used radial velocity and astrometric data to make a convincing case for a binary companion to TYC 3797-01268-1.

Our He I λ10830 line spectrum for this star is very strong: $\log(RW_{He}) = -4.10$ (EW = 867 mÅ). However, the line profile is very unusual for our program stars. In Figure 12 we display the TYC 3797-01268-1 spectrum, and its contrast to the 40-star mean of other strong λ10830 lines is striking. The blue-wing asymmetry discussed in Section 5.3 is a prominent spectral feature of this star. To signal this star's uniqueness we already have labeled its position in Figures 7–9.

Giants with very high lithium abundances and fast rotation can be understood if the Li enhancements have been caused by external events such as mergers with massive planets, brown dwarfs, or compact objects like white dwarfs. An expectation for the merger scenario for Li-rich giants is the presence of dust as a result of mass loss and hence the infrared excess (Denissenkov & Herwig 2004; Carlberg et al. 2010; Zhang & Jeffery 2013). However, IR excess among giants is extremely rare as

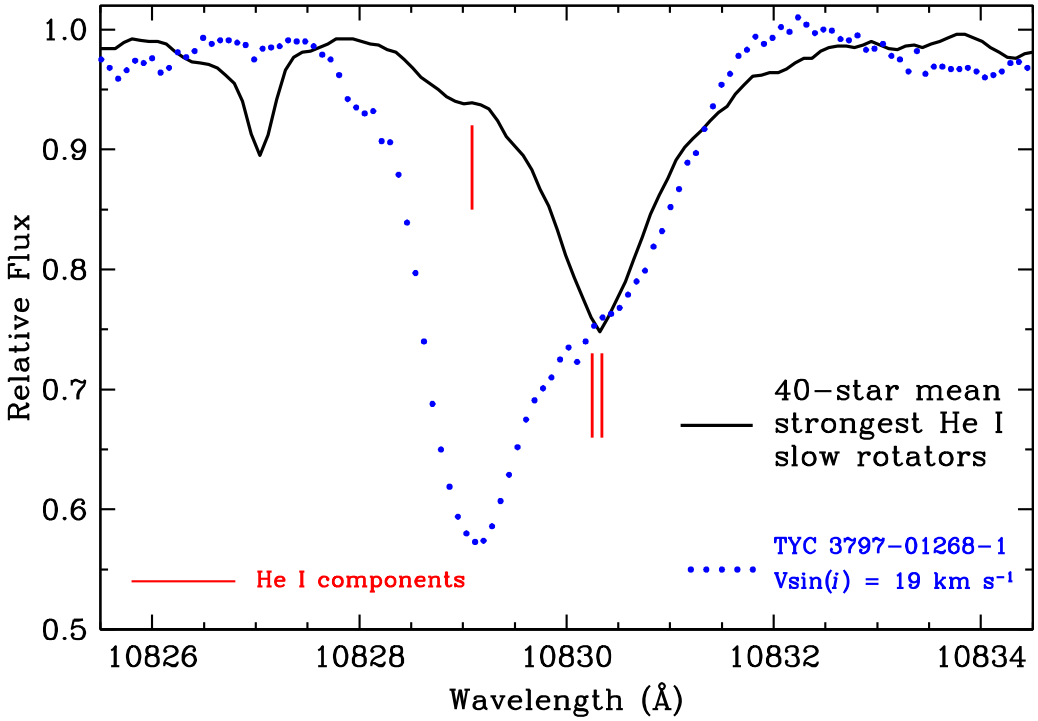

Figure 12. Small section of spectra showing details of the He line profiles. The solid black line represents the mean line profile of the strongest He I λ10830 transitions for program stars without significant rotational broadening. The λ10830 line is a triplet, whose components are marked with vertical red lines. The feature at 10827 Å is a residual of imperfect cancellation of the very strong photospheric Si I line and should be ignored. The dotted blue line shows our single observation of TYC 3797-01288-1. In the figure legend we quote our derived *V*sin(*i*) value. See the text for discussion of this unusual star.

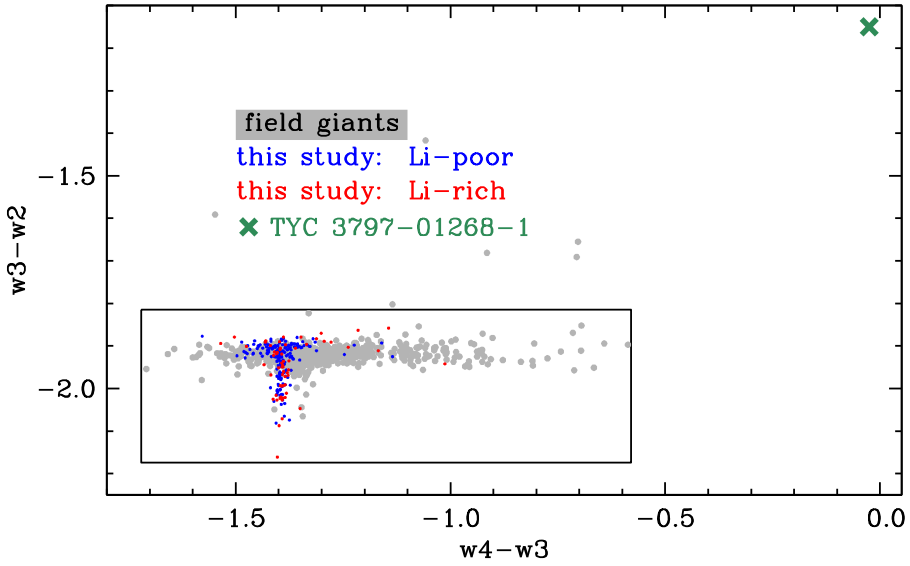

Figure 13. Far-IR color–color plot from WISE. The long rectangular box defines the limits of these colors for red giant stars without IR excesses, as computed by Mallick et al. (2022). Special attention is called TYC 3797-01268-1 with a dark green × symbol. See Section 5.4 for discussion of this star.

shown by various surveys, e.g., Zuckerman et al. (1995),Bharat Kumar et al. (2015), and Mallick et al. (2022). We searched for IR excess among our program stars by using Wide-field Infrared Survey Explorer (WISE; Wright et al. 2010) colors, as detailed in Mallick et al. (2022). Of the 278 giants in our study 262 stars have flux measurements in all four WISE bands (3.3 μ, 4.6 μ, 11.6 μ, 22.1 μm). Figure 13 displays a WISE color–color diagram for red giants in general and for our program stars. This plot is similar to the upper panels of Figure 4 in Mallick et al. In particular, the rectangular box is the theoretical "zero-IR-excess box" computed by them based on the effective temperatures of stars in the red giant/clump temperature domain. Observed colors with larger values of w4–w3 or w3–w2 than the box limits are presumed to be affected by circumstellar disk material.

Inspection of Figure 13 reveals IR excess only in TYC 3797-01268-1. This is in agreement with the Mallick et al. conclusion that Li-rich giants with IR excess are more likely to be fast rotators. Unfortunately, none of their giants are in our current program because their analysis is based on the GALactic

Archaeology with Herschel Multi-tiered Extragalactic Survey in the southern hemisphere, largely inaccessible to HET/HPF observations. To explore this idea more completely, it will be necessary to analyze more rapid rotators among Li-rich giants that have strong λ10830 transitions and IR excess. Our stellar sample, constructed with primary attention to Li abundance, does not fairly represent the rapid-rotation red giant subpopulation. A better survey based on a large $V\sin(i)$ range is appropriate for a future study.

We also constructed flux curves for TYC 3797-01268-1 using broadband colors from optical to far-IR wavelengths (0.4−100 μm) using the spectral energy distribution software package VOSA (Bayo et al. 2008; Rodrigo et al. 2020).[29] Comparison of the observed flux curves to theoretical ones confirms that IR excesses become apparent at wavelengths beyond $\sim$5 μm in this star, a clean signature of a very dusty red giant.

Finally, we also examined individual λ10830 profiles in our sample of rapidly rotating stars. These profile shapes sometimes are uncertain due to significant contamination by neighboring photospheric features, as seen in the right panel of Figure 5. However, almost all of these He I profiles appear to be reasonably symmetric and centered at 10830.3 Å. The single case of a significant blueshifted line profile is TYC 3797-01268-1.

6. Stellar Motions

6.1. Space Velocities

In order to determine whether Li-rich and Li-poor stars belong to different kinematic structures, we obtain three-dimensional (3D) Cartesian velocities from Marchetti (2021). For reference, we define a 3D Cartesian velocity (U, V, W) and position (X, Y, Z) vector for each star whereby U is positive in the direction pointing toward the GC, V is positive along the direction of the disk rotation, and W is positive when pointing toward the North Galactic pole. In this convention, we assume that the Sun's location is (X, Y, Z) = (8.20, 0.00, 0.025) kpc and (U, V, W) = (14.0, 250.24, 7.25) km s^{-1} relative to the Galactic center (e.g., Schönrich 2012). The spatial positions and velocities for the stars in this study are computed using astrometric information from Gaia EDR3[30] (e.g., parallax, proper motion, and sky positions; Gaia Collaboration et al. 2020). The radial velocities are also sourced from Gaia EDR3 (Katz et al. 2019). The astrometric and radial velocity information are then used to derive full 3D positions and velocities using the method outlined in Section 2 of Marchetti (2021). With the 3D velocities for each star, we computed the probability that the star belonged to the thin disk, thick disk, or halo population using the method outline in Section 2.4 of Ramírez et al. (2013).

In Figure 14, we show the $U-V$ kinematic plane (top panel) and the Toomre diagram (bottom panel) for the Li-rich stars (orange 'x's) and Li-poor/normal stars (gray 'x's). From these plots we find that the Li-rich stars and Li-poor (normal) stars are mostly part of the kinematic thin disk, and the two samples do not seem to be significantly different. To quantify this further, we also compute the fractions of Li-rich and Li-poor stars that are parts of the kinematic thick and thin disks using the probabilities defined above. We find that more than 80% of the Li-rich stars have a 70% or higher chance of belonging to the kinematic thin disk. Similarly, $\sim$90% of the Li-normal/poor stars have a 70% or higher chance of belonging to the kinematic thin disk. From this probabilistic kinematic analysis, as well as Figure 14, we can conclude that the sample of Li-rich and Li-poor stars are almost entirely consistent (at the 80%–90% level) of thin disk giant stars. We performed a two-sample Kolmogorov–Smirnov test, finding a p-value of 0.43, on the total velocity distribution for the Li-rich and Li-poor stars. This test allows us to assess the probability that the Li-rich and Li-poor stars are drawn from the same underlying kinematic distribution. The results of this test indicate that there is not sufficient evidence that the Li-rich and Li-normal stars are drawn from different underling kinematic populations. We also find that $\sim$90% of the He strong ($\log(\mathrm{RW_{He}}) > -4.85$) have a 70% or higher chance of belonging to the kinematic thin disk.

6.2. Astrometric Accelerations with Hipparcos and Gaia

In the Adamów et al. (2014) spectroscopic survey, Li was detected in 82 giants, with 11 of them being Li-rich (A(Li) > 1.4). Among these, four showed evidence of stellar or substellar companions based on radial velocity variations. They speculated that excess lithium and binarity may be related, although the underlying basis and statistical validation of any such connection is not yet established. More recently, Gonćalves et al. (2020) and Jorissen et al. (2020) have conducted radial velocity surveys of individual Li-rich stars, with mixed conclusions. Jorissen et al. found no excess binary frequency among their 11 Li-rich giants compared to Li-poor samples. Gonćalves et al. (2020) studied 18 Li-rich stars and detected radial velocity variations in some of them, but suggest that further velocity monitoring work is needed before reaching final conclusions on binarity statistics. Systematic radial velocity campaigns to increase sample sizes would be welcome.

To help assess the binary frequency in our Li-rich stars, we have crossmatched the 278 stars in our program with Gaia EDR3 (Gaia Collaboration et al. 2020) and the Hipparcos–Gaia Catalog of Accelerations (HGCA; Brandt 2018; Brandt 2021). Gaia's renormalized unit weight error (RUWE) value provides information about the goodness of fit of the nominal five-parameter astrometric solution. Values near 1.0 are expected for a typical good fit, whereas values larger than $\approx$1.4 have been shown to indicate the presence of a stellar companion (Stassun & Torres 2021). HGCA makes use of recalibrated proper motions from Hipparcos and Gaia as well as the mean scaled positional difference between the two epochs to measure long-term accelerations (changes in proper motion) over this time period. The most precise acceleration measurement that we make use of in this study is between Gaia and the Hipparcos–Gaia scaled positional difference. The 34 months baseline sampled in Gaia's EDR3 release is most sensitive to companions at separations of a few astronomical unit, whereas the $\approx$25 yr baseline of the HGCA catalog can reveal companions at typical separations of a few to tens of astronomical units (e.g., Brandt et al. 2019; Bowler et al. 2021; Franson et al. 2022). In this way these two methods complement each other to probe stellar and substellar masses at moderate-to-wide separations.[31]

Figure 15 shows the Gaia RUWE values and the SNR values of the HGCA acceleration measurements as a function of the He I λ10830 Å reduced widths. Altogether 275 stars have Gaia

[29] Available at http://svo.cab.inta-csic.es.

[30] We note here that, while the full Gaia DR3 was released in 2022 June, the astrometric information was not updated between the EDR3 and the full DR3.

[31] TYC 3797-01268-1 has Gaia RUWE = 2.81, consistent with its binary status, as discussed by Jorissen et al. (2020), but it does not have an HGCA measurement.

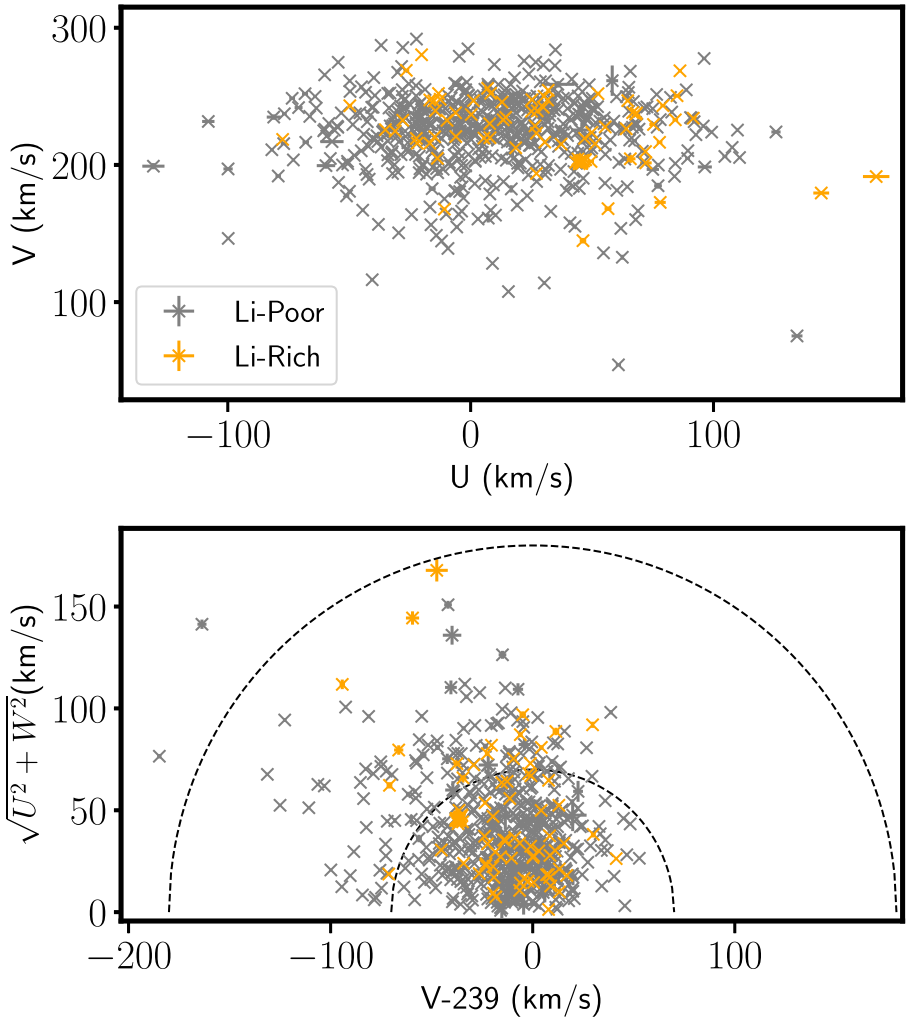

Figure 14. Top panel: $U - V$ velocity plane for Li-rich stars (orange 'x's) and Li-poor stars (gray 'x's). Bottom Panel: Toomre diagram for Li-rich stars and Li-poor stars. In the Toomre diagram panel, we subtract 239 km s^{-1} to place the velocities in the local standard of rest. For reference, the dashed lines represent a constant total velocity of 70 and 180 km s^{-1}, respectively. No significant kinematic difference is detected between the Li-rich and Li-poor populations.

RUWE measurements. Among these, 207 stars have weak helium absorption ($\log(\mathrm{RW_{He}}) < -4.85$), 24 of which have elevated RUWE values above 1.4. This implies a binary occurrence rate of at least $11.9^{+2.4}_{-2.2}$% using a binomial likelihood function. Further, 68 stars have strong helium absorption ($\log(\mathrm{RW_{He}}) > -4.85$); 17 of these have elevated RUWE values, indicating a $25.5^{+5.5}_{-5.0}$% binary occurrence rate. Similarly, 99 bright stars from our program are in the HGCA catalog. For the 68 helium-weak subsample of stars, 11 ($16.8^{4.8}_{4.2}$%) have SNR values above 3 and therefore are likely to have long-term astrometric accelerators (and hence companions). For the helium-strong sample, 11 stars ($36.1^{+8.9}_{-8.1}$%) have SNR values above 3. These binomial posterior probability distributions for the companion frequencies are shown in Figure 16.

In both cases—stars with RUWE values and those with HGCA measurements—the binary occurrence rate is higher for stars with strong helium absorption compared to stars with weak helium. For the RUWE subsample, the significance of the difference is at the $\approx 2.3\sigma$ level. For the HGCA subsample, the difference is at the $\approx 2.0\sigma$ level. This suggests that there is likely (although not definitively) a relationship between the strength of the 10830 Å helium line and stellar multiplicity. Depending on the companion mass, separation, and eccentricity, it is possible that tidal interactions could impact the stellar chromosphere near periastron. Alternatively, if enhanced helium is related to the engulfment of planets, the presence of an outer stellar or substellar companion could indicate that the inner object underwent high-eccentricity tidal migration in the same way that hot Jupiters can form around main-sequence stars (Fabrycky & Tremaine 2007; Dawson & Johnson 2018). In this scenario, Kozai–Lidov oscillations with an outer inclined companion can pump the eccentricity of the inner object until the tidal influence of the host star dampens, circularizes, and decays the planet's orbit. These hypotheses can be tested with a suite of follow-up observations including rotation period measurements of the strong helium stars, radial velocity monitoring, and high-contrast imaging. Gaia's final data release will provide additional clues about the nature of companions in these systems.

6.3. The Motions of Li-poor, He-strong Giants

90% of Li-poor program stars exhibit weak He I λ10830 features. Here we briefly comment on the 10% of Li-poor stars that have strong λ10830 lines. There are 16 stars in this category; 6 of them have astrometric indicators suggestive of the presence of companion objects. All of these stars have Gaia

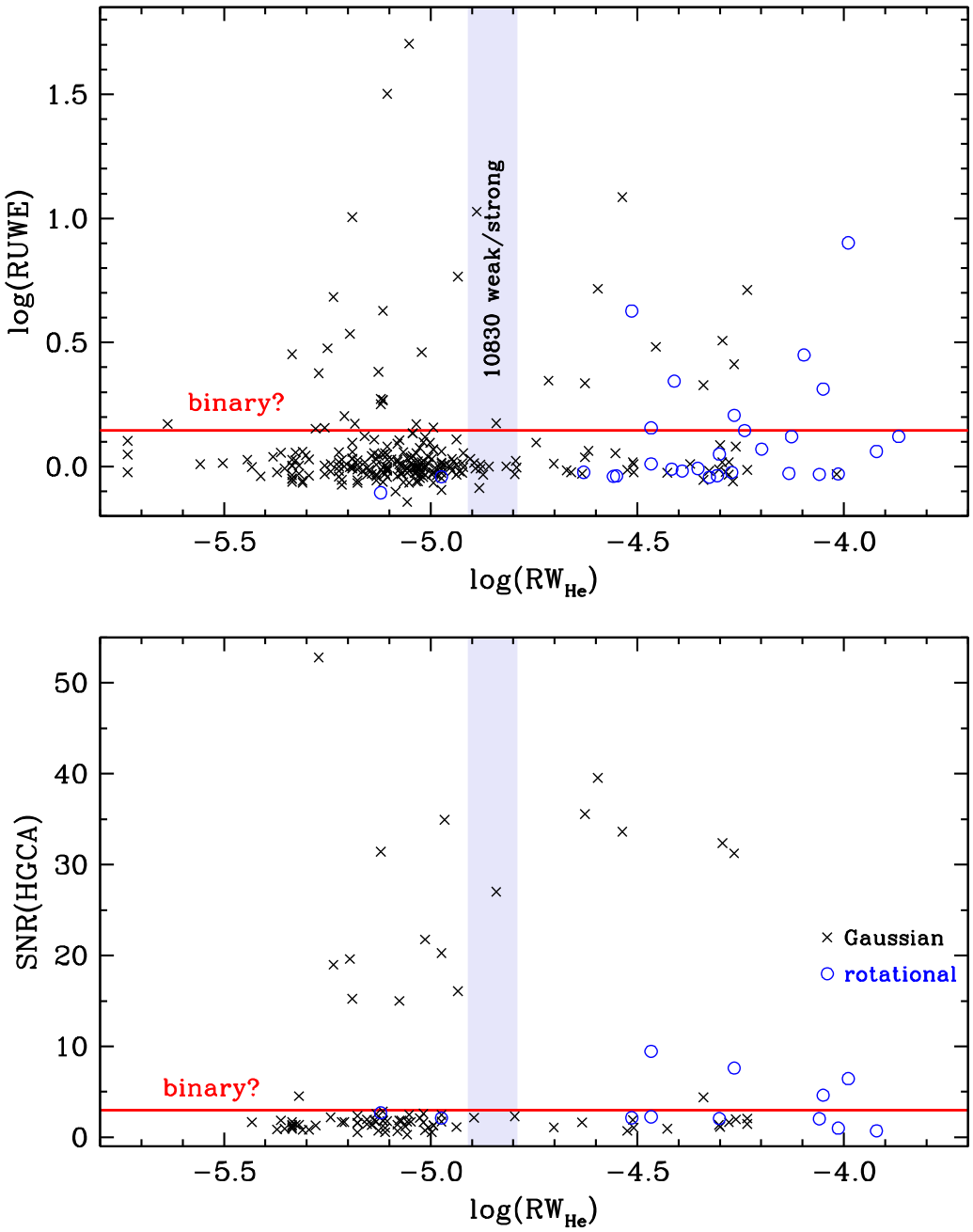

Figure 15. Correlations of log(RW$_{He}$) with the Gaia RUWE (top panel) and HGCA (bottom panel). The symbols are the same as in Figure 9 and noted in the figure legend. The red line in each panel indicates the minimum value of each of these excess astrometric motion indicators that might suggest the presence of binary motion. See the text for more details.

RUWE > 1.4 or HGCA > 3, and 4 of them have HGCA > 3. Further, 2 additional stars, TYC 3304-00101-1 and TYC 3667-01280-1, are known to host giant planets (Niedzielski et al. 2007, 2016); and star TYC 3318-00020-1 is a rapid rotator ($V\sin(i) = 17\,\mathrm{km\,s^{-1}}$). Thus 9 out of 16 Li-poor stars with strong He I lines are known or suspected to have active chromospheres that may be due to present or past binary interactions.

The other 7 stars in this group have no known observational anomalies. It is worth noting that none of these stars has a substantial literature history; their only high-resolution spectroscopic studies appear to be from Adamów et al. (2014) or Afşar et al. (2018). They are worth further study, but we conclude here that the few red giants that are Li-poor but have strong λ10830 lines often can be understood as resulting from binary interactions.

7. Conclusions

This paper has explored the relationship between Li abundances and absorption strengths of He I λ10830 in red giant stars. Our survey considers only observational aspects of the Li–He linkage, from which a few general conclusions may be drawn:

1. 90% of Li-poor stars, defined for this paper as those with $\log\epsilon(\mathrm{Li}) < 1.25$, have weak λ10830 transitions, $\log(\mathrm{RW_{He}}) < -4.85$. In contrast, $\simeq$55% of Li-rich stars have strong λ10830 absorptions.

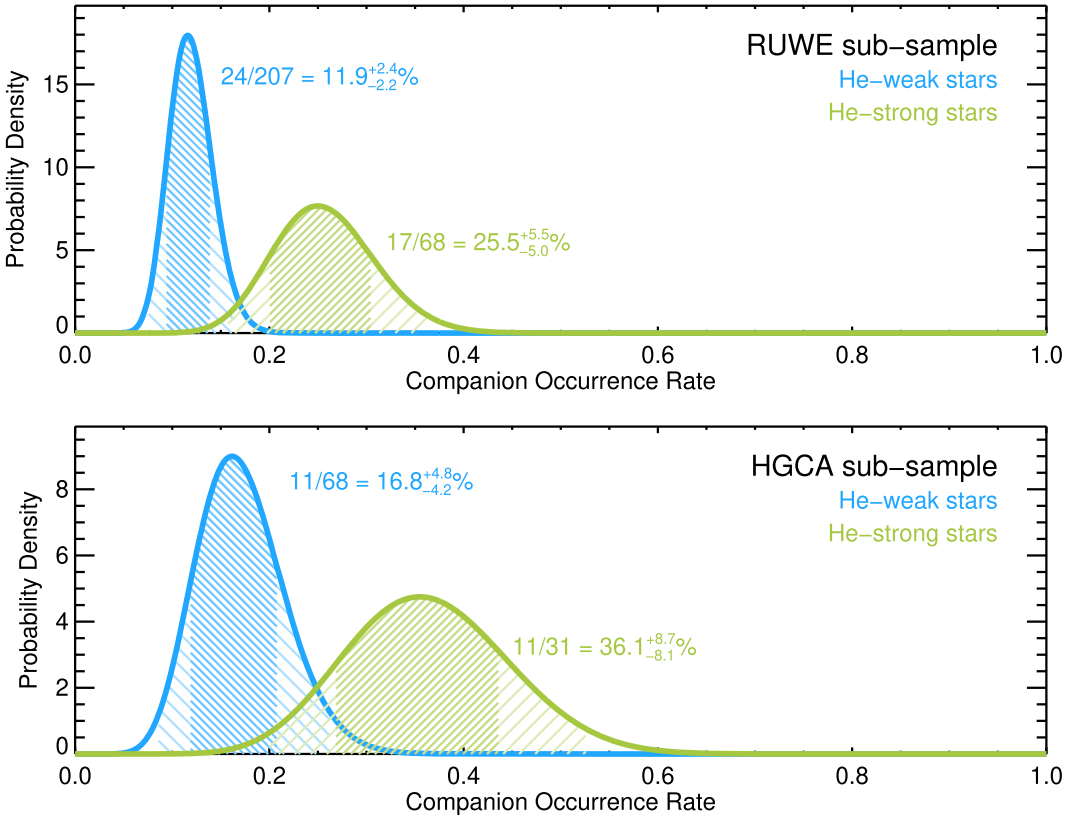

Figure 16. Constraints on the frequency of binary companions for stars in our sample with Gaia RUWE measurements (top) and those with HGCA accelerations (bottom). In both cases, stars with strong helium absorption have a higher companion occurrence rate at the 2.3σ level for the RUWE subsample and at the 2.0σ level for the HGCA subsample.

2. The vast majority of He-strong stars reside on the He-burning RC and RHB.
3. Both Li-rich and He-strong stars are heavily concentrated in the Galactic thin disk based on kinematics.
4. Many of the Li-rich and He-strong stars are also rapid rotators, or have suspected binary companions.
5. About half of the Li-poor, He-strong stars also have evidence for binarity or rapid rotation.
6. From these observational indicators we suggest, in agreement with previous studies, that red giants are most likely to exhibit both high Li abundances and strong He I λ10830 absorption lines if they are He-core-burning RC/RHB stars, and have current and/or past binary companions.

Several follow-up studies are underway to clarify the evolutionary histories of red giants with strong λ10830 absorption lines. The most immediate one is a large-sample survey of Kepler-field red giants. The asteroseismic parameters known for these stars will identify the role of horizontal-branch "age" or time since the helium flash on the Li–He surface combination. In Table 1 we include 13 Kepler giants observed in 2021, but our sample has now grown to 55 stars. A. Mallick et al. (2022, in preparation) will report the He I λ10830 data for this larger sample of Kepler giants with known Li abundances and discuss the evolutionary implications of these stars.

We are undertaking a field star survey based only on red giant rotation to estimate the importance of red giant envelope angular momentum in creating the large λ10830 lines seen in many of our program stars. It will also be worthwhile in the future to investigate λ10830 strengths and Li abundances in binary-suspected giants, those with high values of RUWE and/or HGCA (Figure 15). Finally it would be good to conduct a southern-hemisphere extension to the present survey, which has been limited to $\delta > -10°$. That study could be undertaken with a southern-hemisphere high-resolution 1 μm instrument, such as the Warm Near-Infrared High-Resolution Spectrograph with Very High Throughput (Ikeda et al. 2022), Very Large Telescope Cryogenic High-resolution Infrared Echelle Spectrograph (Kaeufl et al. 2004; Dorn et al. 2014), or PHOENIX (Hinkle et al. 2003).

We thank Claudia Aguilere-Gómez, Bengt Gustafsson, Noriyuki Matsunaga, George Preston, and our referee for helpful comments on this work. These results are based on observations obtained with the Habitable-zone Planet Finder Spectrograph on the Hobby–Eberly Telescope. We thank the Telescope Operators at the HET for the skillful execution of our observations with HPF. The Hobby–Eberly Telescope is a joint project of the University of Texas at Austin, the Pennsylvania State University, Ludwig-Maximilians-Universität München, and Georg-August Universität Gottingen. The HET is named in honor of its principal benefactors, William P. Hobby and Robert E. Eberly. The HET collaboration acknowledges the support and resources from the Texas Advanced Computing Center. We are happy to acknowledge support from NSF grants AST-1616040 (CS), AST-1908892 (GNM), and Technological Research Council of Turkey (TÜBITAK), project No. 112T929 (MA).

Facility: HET (HPF).

Software: linemake (https://github.com/vmplacco/linemake), MOOG (Sneden 1973), IRAF (Tody 1986, 1993), SPECTRE (Fitzpatrick & Sneden 1987), Goldilocks (https://github.com/grzeimann/Goldilocks_Documentation).

ORCID iDs

Christopher Sneden https://orcid.org/0000-0002-3456-5929
Melike Afşar https://orcid.org/0000-0002-2516-1949
Zeynep Bozkurt https://orcid.org/0000-0002-4413-4401
Monika Adamów https://orcid.org/0000-0002-6904-359X
Anohita Mallick https://orcid.org/0000-0002-4282-605X
Bacham E. Reddy https://orcid.org/0000-0001-9246-9743
Steven Janowiecki https://orcid.org/0000-0001-9165-8905
Suvrath Mahadevan https://orcid.org/0000-0001-9596-7983
Brendan P. Bowler https://orcid.org/0000-0003-2649-2288
Keith Hawkins https://orcid.org/0000-0002-1423-2174
Karin Lind https://orcid.org/0000-0002-8892-2573
Andrea K. Dupree https://orcid.org/0000-0002-8985-8489
Joe P. Ninan https://orcid.org/0000-0001-8720-5612
Neel Nagarajan https://orcid.org/0000-0002-7112-2086
Cynthia S. Froning https://orcid.org/0000-0001-8499-2892
Chad F. Bender https://orcid.org/0000-0003-4384-7220
Ryan Terrien https://orcid.org/0000-0002-4788-8858
Lawrence W. Ramsey https://orcid.org/0000-0002-4289-7958
Gregory N. Mace https://orcid.org/0000-0001-7875-6391

References

Adamów, M., Niedzielski, A., Kowalik, K., et al. 2018, A&A, 613, A47
Adamów, M., Niedzielski, A., Villaver, E., et al. 2015, A&A, 581, A94
Adamów, M., Niedzielski, A., Villaver, E., Wolszczan, A., & Nowak, G. 2014, A&A, 569, A55
Afşar, M., Bozkurt, Z., Böcek Topcu, G., et al. 2018, AJ, 155, 240
Afšar, M., Sneden, C., Wood, M. P., et al. 2018, ApJ, 865, 44
Aguilera-Gómez, C., Chanamé, J., Pinsonneault, M. H., & Carlberg, J. K. 2016, ApJ, 829, 127
Alexander, J. B. 1967, Obs, 87, 238
Balachandran, S. C., Fekel, F. C., Henry, G. W., & Uitenbroek, H. 2000, ApJ, 542, 978
Bayo, A., Rodrigo, C., Barrado y Navascues, D., et al. 2008, A&A, 492, 277
Bharat Kumar, Y., Reddy, B. E., Muthumariappan, C., & Zhao, G. 2015, A&A, 577, A10
Bizyaev, D., Smith, V. V., & Cunha, K. 2010, AJ, 140, 1911
Boesgaard, A. M., & Tripicco, M. J. 1986, ApJL, 302, L49
Boesgaard, A. M., & Tripicco, M. J. 1987, ApJ, 313, 389
Bowler, B. P., Endl, M., Cochran, W. D., et al. 2021, ApJL, 913, L26
Brandt, T. D. 2018, ApJS, 239, 31
Brandt, T. D. 2021, ApJS, 254, 42
Brandt, T. D., Dupuy, T. J., & Bowler, B. P. 2019, AJ, 158, 140
Brooke, J. S. A., Bernath, P. F., Western, C. M., et al. 2016, JQSRT, 168, 142
Brown, J. A., Sneden, C., Lambert, D. L., & Dutchover, E. J. 1989, ApJS, 71, 293
Cameron, A. G. W., & Fowler, W. A. 1971, ApJ, 164, 111
Carlberg, J. K., Cunha, K., Smith, V. V., & Majewski, S. R. 2012, ApJ, 757, 109
Carlberg, J. K., Smith, V. V., Cunha, K., Majewski, S. R., & Rood, R. T. 2010, ApJL, 723, L103
Carrera, R., Bragaglia, A., Cantat-Gaudin, T., et al. 2019, A&A, 623, A80
Casamiquela, L., Blanco-Cuaresma, S., Carrera, R., et al. 2019, MNRAS, 490, 1821
Casey, A. R., Ho, A. Y. Q., Ness, M., et al. 2019, ApJ, 880, 125
Ceillier, T., Tayar, J., Mathur, S., et al. 2017, A&A, 605, A111
Charbonnel, C., Lagarde, N., Jasniewicz, G., et al. 2020, A&A, 633, A34
Costa, A. D., Canto Martins, B. L., Bravo, J. P., et al. 2015, ApJL, 807, L21
Cranmer, S. R. 2009, LRSP, 6, 3
Dawson, R. I., & Johnson, J. A. 2018, ARA&A, 56, 175
de Laverny, P., do Nascimento, J. D. J., Lèbre, A., & De Medeiros, J. R. 2003, A&A, 410, 937
De Medeiros, J. R., Udry, S., Burki, G., & Mayor, M. 2002, A&A, 395, 97
Deepak, & Lambert, D. L. 2021, MNRAS, 507, 205
Deepak, L. D. L., & Reddy, B. E. 2020, MNRAS, 494, 1348
Deepak, R. B. E. 2019, MNRAS, 484, 2000
Deka-Szymankiewicz, B., Niedzielski, A., Adamczyk, M., et al. 2018, A&A, 615, A31
Den Hartog, E. A., Lawler, J. E., Sneden, C., et al. 2021, ApJS, 255, 27
Denissenkov, P. A., & Herwig, F. 2004, ApJ, 612, 1081
Donor, J., Frinchaboy, P. M., Cunha, K., et al. 2018, AJ, 156, 142
Dorn, R. J., Anglada-Escude, G., Baade, D., et al. 2014, Msngr, 156, 7
Dupree, A. K., Penn, M. J., & Jones, H. P. 1996, ApJL, 467, L121
Dupree, A. K., Sasselov, D. D., & Lester, J. B. 1992, ApJL, 387, L85
Fabrycky, D., & Tremaine, S. 2007, ApJ, 669, 1298
Fekel, F. C., Webb, R. A., White, R. J., & Zuckerman, B. 1996, ApJL, 462, L95
Fitzpatrick, M. J., & Sneden, C. 1987, BAAS, 19, 1129
Franson, K., Bowler, B. P., Brandt, T. D., et al. 2022, AJ, 163, 50
Gaia Collaboration, Brown, A. G. A., Vallenari, A., et al. 2020, A&A, 649, A1
Girardi, L., Groenewegen, M. A. T., Weiss, A., & Salaris, M. 1998, MNRAS, 301, 149
Gonćalves, B. F. O., da Costa, J. S., de Almeida, L., Castro, M., & do Nascimento, J. D. J. 2020, MNRAS, 498, 2295
Gray, D. F. 2008, The Observation and Analysis of Stellar Photospheres (Cambridge: Cambridge Univ. Press)
Guillout, P., Klutsch, A., Frasca, A., et al. 2009, A&A, 504, 829
Hanni, L. 1984, SvAL, 10, 51
Harvey, J. W., Krieger, A. S., Timothy, A. F., & Vaiana, G. S. 1975, OMOAA, 104, 50
Hinkle, K., & Wallace, L. 2005, in ASP Conf. Ser. 336, Cosmic Abundances as Records of Stellar Evolution and Nucleosynthesis, ed. T. G. Barnes, III & F. N. Bash (San Francisco, CA: ASP), 321
Hinkle, K. H., Blum, R. D., Joyce, R. R., et al. 2003, Proc. SPIE, 4834, 353
Høg, E., Fabricius, C., Makarov, V. V., et al. 2000, A&A, 355, L27
Iben, I., Jr. 1967, ApJ, 147, 624
Ikeda, Y., Kondo, S., Otsubo, S., et al. 2022, PASP, 134, 015004
Jofré, E., Petrucci, R., García, L., & Gómez, M. 2015, A&A, 584, L3
Jorissen, A., Van Winckel, H., Siess, L., et al. 2020, A&A, 639, A7
Kaempf, T. A., de Boer, K. S., & Altmann, M. 2005, A&A, 432, 879
Kaeufl, H.-U., Ballester, P., Biereichel, P., et al. 2004, Proc. SPIE, 5492, 1218
Katz, D., Sartoretti, P., Cropper, M., et al. 2019, A&A, 622, A205
Kramida, A. 2019, APS Division of Atomic, Molecular and Optical Physics Meeting, 2019, N09.004
Kramida, A., Ralchenko, Y., Reader, J. & NIST ASD Team 2019, NIST Atomic Spectra Database v5.7.1, doi:10.18434/T4W30F
Kriskovics, L., Kővári, Z., Vida, K., Granzer, T., & Oláh, K. 2014, A&A, 571, A74
Kumar, Y. B., & Reddy, B. E. 2020, JApA, 41, 49
Kumar, Y. B., Reddy, B. E., Campbell, S. W., et al. 2020, NatAs, 4, 1059
Kumar, Y. B., Reddy, B. E., & Lambert, D. L. 2011, ApJL, 730, L12
Kurucz, R. L. 2011, CaJPh, 89, 417
Kurucz, R. L. 2018, in ASP Conf. Ser. 515, Workshop on Astrophysical Opacities, ed. C. Mendoza, S. Turck-Chiéze, & J. Colgan (San Francisco, CA: ASP), 47
Lambert, D. L., Dominy, J. F., & Sivertsen, S. 1980, ApJ, 235, 114
Lodders, K. 2021, SSRv, 217, 44
Luck, R. E. 1982, PASP, 94, 811
Lyubimkov, L. S., Lambert, D. L., Kaminsky, B. M., et al. 2012, MNRAS, 427, 11
Mahadevan, S., Ramsey, L., Bender, C., et al. 2012, Proc. SPIE, 8446, 84461S
Mahadevan, S., Ramsey, L. W., Terrien, R., et al. 2014, Proc. SPIE, 9147, 91471G
Mallick, A., Reddy, B. E., & Muthumariappan, C. 2022, MNRAS, 511, 3741
Marchetti, T. 2021, MNRAS, 503, 1374
Martell, S. L., Simpson, J. D., Balasubramaniam, A. G., et al. 2021, MNRAS, 505, 5340
Massarotti, A., Latham, D. W., Stefanik, R. P., & Fogel, J. 2008, AJ, 135, 209
Mermilliod, J.-C. 1995, in Information On-line Data in Astronomy, ed. D. Egret & M. A. Albrecht, Vol. 203 (Dordrecht: Springer), 127
Mott, A., Steffen, M., Caffau, E., Spada, F., & Strassmeier, K. G. 2017, A&A, 604, A44
Niedzielski, A., Deka-Szymankiewicz, B., Adamczyk, M., et al. 2016, A&A, 589, C1
Niedzielski, A., Konacki, M., Wolszczan, A., et al. 2007, ApJ, 669, 1354
Ninan, J. P., Bender, C. F., Mahadevan, S., et al. 2018, Proc. SPIE, 10709, 107092U

O'Brien, G. T. J., & Lambert, D. L. 1986, ApJS, 62, 899
Overbeek, J. C., Friel, E. D., Jacobson, H. R., et al. 2015, AJ, 149, 15
Pilachowski, C. 1986, ApJ, 300, 289
Placco, V. M., Sneden, C., Roederer, I. U., et al. 2021, Linemake: Line List Generator, Astrophysics Source Code Library, ascl:2104.027
Preston, G. W., Sneden, C., & Chadid, M. 2022, AJ, 163, 109
Ramírez, I., & Allende Prieto, C. 2011, ApJ, 743, 135
Ramírez, I., Allende Prieto, C., & Lambert, D. L. 2013, ApJ, 764, 78
Ramírez, I., & Meléndez, J. 2005, ApJ, 626, 465
Randich, S., Pasquini, L., Franciosini, E., et al. 2020, A&A, 640, L1
Rebull, L. M., Carlberg, J. K., Gibbs, J. C., et al. 2015, AJ, 150, 123
Reddy, A. B. S., & Lambert, D. L. 2016, A&A, 589, A57
Rodrigo, C., Bayo Arán, A., Solano, E., & Cortés-Contreras, M. 2020, in XIV.0 Scientific Meeting (Virtual) of the Spanish Astronomical Society, 181
Romano, D., Magrini, L., Randich, S., et al. 2021, A&A, 653, A72
Sanz-Forcada, J., & Dupree, A. K. 2008, A&A, 488, 715
Schönrich, R. 2012, MNRAS, 427, 274
Singh, R., Bharat Kumar, Y., Reddy, B. E., & Aoki, W. 2020, MNRAS, 491, 3838
Singh, R., Reddy, B. E., Bharat Kumar, Y., & Antia, H. M. 2019a, ApJL, 878, L21
Singh, R., Reddy, B. E., Campbell, S. W., Kumar, Y. B., & Vrard, M. 2021, ApJL, 913, L4
Singh, R., Reddy, B. E., & Kumar, Y. B. 2019b, MNRAS, 482, 3822
Sneden, C. 1973, ApJ, 184, 839
Sneden, C., Afšar, M., Bozkurt, Z., et al. 2021, AJ, 161, 128
Stassun, K. G., & Torres, G. 2021, ApJL, 907, L33
Takeda, Y., & Tajitsu, A. 2017, PASJ, 69, 74
Tody, D. 1986, Proc. SPIE, 627, 733
Tody, D. 1993, in ASP Conf. Ser. 52, Astronomical Data Analysis Software and Systems II, ed. R. J. Hanisch, R. J. V. Brissenden, & J. Barnes (San Francisco, CA: ASP), 173
Uesugi, A., & Fukuda, I. 1970, MmKyo, 33, 205
Wallerstein, G., & Conti, P. S. 1969, ARA&A, 7, 99
Wallerstein, G., & Helfer, H. L. 1959, ApJ, 129, 720
Wallerstein, G., & Sneden, C. 1982, ApJ, 255, 577
Wenger, M., Ochsenbein, F., Egret, D., et al. 2000, A&AS, 143, 9
Wright, E. L., Eisenhardt, P. R. M., Mainzer, A. K., et al. 2010, AJ, 140, 1868
Yan, H.-L., Shi, J.-R., Zhou, Y.-T., et al. 2018, NatAs, 2, 790
Yan, H.-L., Zhou, Y.-T., Zhang, X., et al. 2021, NatAs, 5, 86
Zarro, D. M., & Zirin, H. 1986, ApJ, 304, 365
Zhang, X., & Jeffery, C. S. 2013, MNRAS, 430, 2113
Zhou, Y. T., Shi, J. R., Yan, H. L., et al. 2018, A&A, 615, A74
Zieliński, P., Niedzielski, A., Wolszczan, A., Adamów, M., & Nowak, G. 2012, A&A, 547, A91
Zirin, H. 1982, ApJ, 260, 655
Zuckerman, B., Kim, S. S., & Liu, T. 1995, ApJL, 446, L79